

Highly Sensitive Refractive Index Nano Sensors with Applications in Glucose Level Detection, and Gas Sensing

By

Sabrina Saima	-180021336
Irina Anjum Pranti	-180021137
Sheza Aini Mumu	-180021332
Umama Kamrul Saifa	-180021334

A Thesis Submitted to the Academic Faculty in Partial Fulfillment of the Requirements for the Degree of

BACHELOR OF SCIENCE IN ELECTRICAL AND ELECTRONIC ENGINEERING

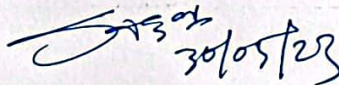


Department of Electrical and Electronic Engineering
Islamic University of Technology (IUT)
Gazipur, Bangladesh
June 2023

Certificate of Approval

The thesis with the title of “Highly Sensitive Refractive Index Nano Sensors with Applications in Glucose Level Detection, Dengue Virus Detection, and Gas Sensing” submitted by Sabrina Saima (180021336), Irina Anjum Pranti (180021137), Sheza Aini Mumu (180021332), Umama Kamrul Saifa (180021334) has been satisfactory and accepted as partial fulfillment of the requirements for the degree of Bachelor of Science in Electrical and Electronic Engineering at Islamic University of Technology (IUT).

Approved by:



30/05/23

Prof. Dr. Rakibul Hasan Sagor
Thesis Supervisor
Professor
Department of Electrical and Electronic Engineering
Islamic University of Technology

Table of Contents

Certificate of Approval	i
Declaration of Authorship	ii
Acknowledgments	iii
List of Figures	iv
List of Abbreviations	vii
List of Tables	vii
Abstract	viii
1. Introduction	1
1.1 Surface Plasmon Polaritons (SPPs)	1
1.2 Waveguide Topologies	2
1.3 Plasmonic Refractive Index Sensor	3
1.4 Literature Review	3
1.5 Thesis Objective	8
1.6 Thesis Layout	9
2. Wave Theory	10
2.1 Maxwell's Equation	10
2.2 Constitutive Equations	11
2.3 Finite-Difference Time Domain (FDTD)	12
2.4 Finite Integration Technique (FIT)	24
3. Plasmonic Materials	15
3.1 Refractive Index and Complex Permittivity	15
3.2 Plasmonic Material Modeling	16
3.3 Drude Model	17
3.4 The Drude-Lorentz Model	17
3.5 Plasmonic Properties of Silver	18

3.6 Performance Matrix: Sensitivity	20
4. Re-simulation of Existing Papers	21
4.1 Re-Simulation with COMSOL Multiphysics	21
4.2 Concentric Triple Ring Resonator	21
4.3 Ring-Type Pentagonal Resonator	22
5. Plasmonic Sensor Design and Performance Analysis	24
5.1 Refractive Index Sensors	24
5.2 Refractive Index Sensor with MIM Waveguide	25
5.3 Our Proposed Structure with Semi-Circular Cavity	25
5.3.1 Basic Structure	25
5.3.2 Initial Results	26
5.3.3 Optimization of Initial Parameters	29
5.3.4 Application	33
5.3.4.1 Application as a Glucose Sensor	34
5.3.4.2 Application as a Cancer Biomarker	36
5.3.5 Conclusion	38
5.4 Our Proposed Structure 2	38
5.4.1 Basic Structure	38
5.4.2 Initial Results	40
5.4.3 Optimization of Initial Parameters	46
5.4.4 Conclusion	55
6. Conclusion and Future Works	61
6.1 Conclusion	61
6.2 Future Works	62
References	63

Declaration of Authorship

We, Sabrina Saima (180021336), Irina Anjum Pranti (180021137), Sheza Aini Mumu (180021332), Umama Kamrul Saifa (180021334), declare that the thesis titled, "Highly Sensitive Refractive Index Nano Sensors with Applications in Glucose Level Detection, and Gas Sensing" and the works presented in it are our own. We verify that this work has been done for the partial fulfillment of the requirements for the degree of Bachelor of Science in Electrical and Electronic Engineering at the Islamic University of Technology (IUT). This thesis report or any part of it has not been submitted elsewhere for the degree for any Degree or Diploma. We have always clearly attributed the sources when we have consulted the published work of others.

Submitted by:

Sabrina Saima

Student ID: 180021336

Irina Anjum Pranti

Student ID: 180021137

Sheza Aini Mumu

Student ID: 180021332

Umama Kamrul Saifa

Student ID: 180021334

Acknowledgements

First and foremost, we would like to express our sincere gratitude to the Almighty Allah (SWT), the most merciful and compassionate, for granting us the strength and perseverance to complete this thesis.

We would like to extend our heartfelt appreciation to our esteemed thesis supervisor, Prof. Dr. Rakibul Hasan Sagor, in the Department of Electrical and Electronic Engineering at the Islamic University of Technology (IUT). His invaluable guidance, unwavering support, and insightful suggestions have been instrumental in shaping our research work. His expertise and mentorship have been a source of inspiration throughout this journey, and we are truly grateful for his continuous encouragement and motivation.

We would also like to express our gratitude to our teachers, Mr. Md. Farhad Hassan and Mr. Infitar Tathfif, and Mr. Rabiul Al Mahmud for their valuable guidance and teachings during the initial stages of our research. Their dedication and expertise have laid a strong foundation for our understanding of the research process.

Furthermore, we extend our thanks to all the faculty members of the Electrical and Electronic Engineering Department at the Islamic University of Technology (IUT) for their support and inspiration. Their knowledge, expertise, and encouragement have played a vital role in our academic and research endeavors.

Lastly, we would like to convey our heartfelt appreciation to our families for their relentless support, understanding, and encouragement throughout the writing of this thesis. Their love, patience, and belief in our abilities have been a constant source of motivation.

Sabrina Saima
Irina Anjum Pranti
Sheza Aini Mumu
Umama Kamrul Saifa
June,2023

List of Figures

1. **Figure 1.1** SPP propagation along the metal-dielectric interface
2. **Figure 1.2.** IMI Waveguide
3. **Figure 1.3.** MIM Waveguide
4. **Figure 3.1.** Sensitivity
5. **Figure 4.1.** Power transmission characteristic of the designed structure
6. **Figure 4.2** Transmittance spectrum for different refractive indices
7. **Figure 4.3** Power transmission characteristic of the designed structure
8. **Figure 4.4** Transmittance spectrum for different refractive indices
9. **Figure 5.1** Two-dimensional (2D) schematic of the proposed RI sensor 1
10. **Figure 5.2** The transmittance peaks obtained for the initial parameters at 1283 nm
11. **Figure 5.3** Variation of refractive index, n , on the initial transmittance profile
12. **Figure 5.4** Normalized Electric Field (V/m) at frequencies
13. **Figure 5.5** Transmittance spectrum for different length of the cavity, L_r
14. **Figure 5.6** Transmittance spectrum for different width of the semi-circle, W_c .
15. **Figure 5.7** Transmittance spectrum for different distance between wavelength and resonator, D
16. **Figure 5.8** Transmittance spectrum for different baffle, G
17. **Figure 5.9** Transmittance spectrum for different refractive indices with the most optimized structural parameters.
18. **Figure 5.10** Transmittance spectrum for different values of low glucose concentration
19. **Figure 5.11** Transmittance spectrum for different values of high glucose concentration
20. **Figure 5.12** Performance of the optimized sensor for detecting (a) Skin Cancer, (b) Breast Cancer, (c) Blood Cancer
21. **Figure 5.13** Two-dimensional (2D) schematic of the proposed RI sensor
22. **Figure 5.14** The transmittance peaks obtained for the initial parameters for 1 to 1.05 refractive index between wavelength 2000 nm to 4000 nm
23. **Figure 5.15** The transmittance peaks obtained for the initial parameters for 1 to 1.05 refractive index between wavelength 800 nm to 2000 nm

24. **Figure 5.16** The transmittance peaks obtained for the initial parameters for 1.2 to 1.3 refractive index between wavelength 1200 nm to 2200 nm
25. **Figure 5.17** The transmittance peaks obtained for the initial parameters for 1.3 to 1.4 refractive index between wavelength 1400 nm to 2400 nm
26. **Figure 5.18** The transmittance peaks obtained for the initial parameters for 1.4 to 1.5 refractive index between wavelength 1400 nm to 3000 nm
27. **Figure 5.19** Transmittance spectrum for different diameter of outer semicircle, L_r
28. **Figure 5.20** Transmission spectrum for different values of n between 1 to 1.05 at L_r (a) 400 nm, (b) 410 nm (c) 420 nm (d) 430 nm_
29. **Figure 5.21** Sensitivity Comparison for different Values of L_r
30. **Figure 5.22** Transmittance spectrum for different diameter of outer semicircle, L_r
31. **Figure 5.23** Transmission spectrum for different values of n between 1 to 1.05 at L_r (a) 398 nm, (b) 399 nm
32. **Figure 5.24** Sensitivity comparison for different values of L_r
33. **Figure 5.25** Transmittance spectrum for different width of the waveguide, W
34. **Figure 5.26** Transmission spectrum for different values of n between 1 to 1.05 at W (a) 20 nm, (b) 30 nm (c) 40 nm (d) 50 nm
35. **Figure 5.27** Sensitivity comparison for different values of W
36. **Figure 5.28** Transmittance spectrum for different radius of the inner circle, R_1
37. **Figure 5.29** Transmission spectrum for different values of n between 1 to 1.05 at R_1 (a) 150 nm, (b) 151 nm
38. **Figure 5.30** Transmission spectrum for different values of n between 1 to 1.05 at R_1 (a) 152 nm, (b) 153 nm (c) 154 nm
39. **Figure 5.31** Sensitivity comparison for different values of R_1
40. **Figure 5.32** Transmittance spectrum for different width of the outer semi-circular cavity, W_1
41. **Figure 5.33** Transmission spectrum for different values of n between 1 to 1.05 at W_1 (a) 23 nm, (b) 24 nm (c) 25 nm (d) 26 nm
42. **Figure 5.34** Sensitivity comparison for different values of W_1
43. **Figure 5.35** Transmittance spectrum for different width of the inner semi-circular cavity, W_2

44. **Figure 5.36** Transmission spectrum for different values of n between 1 to 1.05 at W_2 (a) 29 nm, (b) 30 nm
45. **Figure 5.37** Sensitivity comparison for different values of W_2

List of Abbreviations

1. **SPP** – Surface Plasmon Polariton
2. **IMI** – Insulator Metal Insulator
3. **MIM** – Metal Insulator Metal
4. **RI** – Refractive Index
5. **FOM** – Figure of Merit
6. **RIU** – Refractive Index Unit
7. **DMD** – Dielectric Metal Dielectric

List of Tables

1. **Table 1.1:** Comparison of different shapes resonators sensitivity and FOM **3**
2. **Table 3.1:** Different parameters of Drude model and Lorentz-Drude model and their values for silver **18**
3. **Table 5.1** Initial structural Parameters of the sensor **27**
4. **Table 5.2** Optimized structural Parameters of the sensor **33**
5. **Table 5.3** Sensitivity Analysis for Different Values of Low Glucose Concentration **35**
6. **Table 5.4** Sensitivity Analysis for Different Values of High Glucose Concentration **36**
7. **Table 5.5:** Performance of the optimized sensor as a cancer biomarker[cita] **37**
8. **Table 5.6** Initial structural Parameters of the sensor **39**
9. **Table 5.7** Sensitivity Analysis for $n=1$ to 1.05 between 2000 nm to 4000 nm **40**
10. **Table 5.8** Sensitivity Analysis for $n=1$ to 1.05 between 2000 nm to 4000 nm **42**
11. **Table 5.9** Sensitivity Analysis for $n=1.2$ to 1.3 between 1200 nm to 2200 nm **44**
12. **Table 5.10** Optimized structural Parameters of the sensor **59**

Abstract

This thesis investigates the design, simulation, and performance evaluation of two distinct structures for highly sensitive refractive index sensors based on Metal-Insulator-Metal (MIM) waveguides. The first structure consists of a semi-circular ring with a baffle, while the second structure incorporates double concentric semi-circular rings. Both sensors utilize specifically designed cavities to hold the material under sensing (MUS), with silver filling the surrounding area. The Finite Element Method (FEM) implemented in COMSOL Multiphysics enables numerical analysis of the proposed models and demonstrates the linear relationship between the refractive index and the corresponding shift in the resonant wavelength. In the first structure, extensive simulations and parameter optimization are performed to achieve maximum sensitivity. By tuning the structural parameters, including L_r , W_c , G , and D , to optimized values of 440 nm, 29 nm, 25 nm, and 20 nm respectively, the sensor achieves a remarkable maximum sensitivity of 4859 nm/RIU within the refractive index range of 1.5 to 1.6. Furthermore, the sensor exhibits a high sensitivity of 4255 nm/RIU when detecting different concentrations of glucose solutions. These results establish the sensor's potential for on-chip bio-sensing and chemical applications due to its exceptional sensitivity, straightforward architecture, cost-efficiency, and promising performance as a glucometer. Building upon the success of the first structure, the second structure with double concentric semi-circular rings is developed. By carefully designing the structural parameters, such as the outer semicircle diameter (L_r) at 399 nm, waveguide width (W) at 20 nm, inner circle radius (R_1) at 154 nm, and widths of the outer and inner semi-circular cavity sections (W_1 and W_2) at 26 nm and 29 nm respectively, the sensor achieves a maximum sensitivity of 11573 nm/RIU within the refractive index range of 1 to 1.05, making it particularly suitable for gas sensing applications. Moreover, satisfactory performance is observed across other refractive index ranges relevant to various biosensing regions, including 1.2 to 1.3, 1.3 to 1.4, and 1.4 to 1.5. Both structures capitalize on the linear relationship between the refractive index of the medium and the resonant wavelength, enabling the identification and characterization of unknown materials. By filling the concentric semi-circular cavities with different unknown solutions, a linear shift in the transmission peak is observed, providing valuable information about the refractive index of these solutions. In conclusion, the optimized designs of these refractive index sensors showcase exceptional performance and hold significant potential for gas sensing and biosensing applications. Their ability to accurately detect and analyze unknown substances positions them as promising candidates for a wide range of chemical and biological sensing applications.

Chapter 1

Introduction

1.1 Surface Plasmon Polaritons(SPPs):

Over recent years, researchers have shown their interest in the optical structures where surface plasmon polaritons (SPPs) can propagate. Surface plasmon polaritons, this term has two parts, surface plasmons, and polariton. Surface plasmons are the electron oscillation at the metal surface, and polaritons are the electromagnetic field on the dielectric surface. So, SPPs are formed when the light incident on a dielectric metal junction and propagates like a wave along the metal and a dielectric interface [1]. SPPs are the foundation of plasmonics.

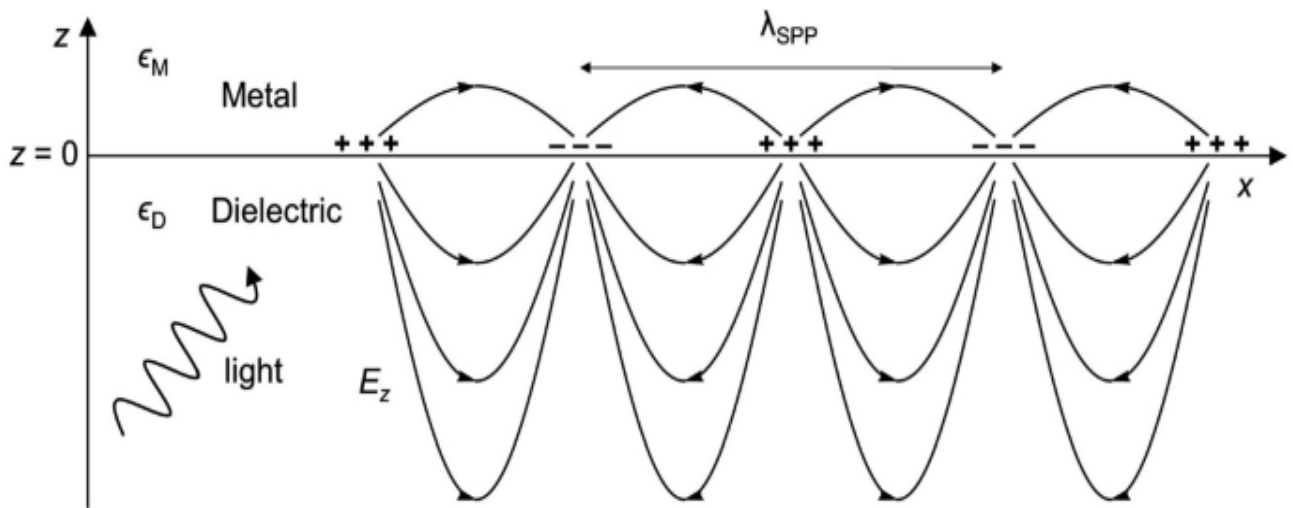


Figure 1.1. SPP propagation along the interface of metal and dielectric [2]

In **Figure 1.1.** the SPP propagation along the metal-dielectric interface is depicted, where the blue area refers to the metal, and the white zone is the dielectric element.

Here electron oscillations on the metal surface and electromagnetic fields on the dielectric surface have been attributed as surface plasmons and polaritons, respectively [1], [3]. Characterized by an exponentially decaying profile in the perpendicular direction [4] and with the ability to modulate light in the deep subwavelength range, SPPs have shown the potential to overcome the diffraction

limit of light [1], [5], [6]. Therefore, SPPs have been implemented to make highly integrated optical devices like refractive index sensors [1], [3]–[5], [7]–[9], demultiplexers [6], biosensors [1], and filters [10].

1.2 Waveguide Topologies:

The most common nanostructures to guide SPPs are Insulator-Metal-Insulator (IMI) and Metal-Insulator-Metal (MIM) waveguides. **Figure 1.2.** depicts the IMI structure where the metal part is sandwiched between two insulators. IMI structure provides better performance in case of long-distance transmission and it has lower propagation loss.

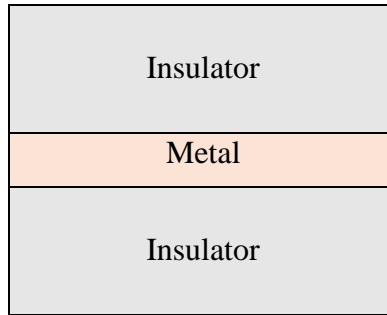


Figure 1.2. IMI Waveguide

Figure 3. depicts the MIM structure where the insulator part is sandwiched between two insulators. MIM structure has higher propagation loss. Even with this disadvantage of MIM structure, recently they have been highly considered as compact plasmonic waveguide structures because of their propagation lengths, ease of fabrication, and the potential to generate strong field confinement [3], [5], [7]. MIM structured waveguide can be used to transmit optical and electrical signals, embedding conventional electronic and photonic circuits on the same chip structure [1], [3].

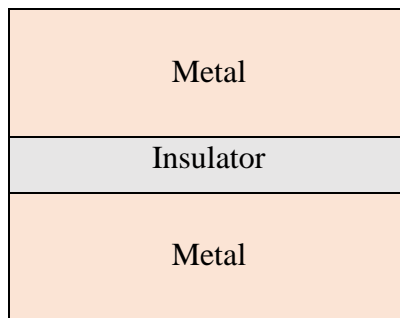


Figure 3. MIM Waveguide

As the MIM waveguide has higher field confinement characteristics it shows better performance in the case of designing Refractive Index (RI) sensors.

1.3 Plasmonic Refractive Index Sensor:

Plasmonics refractive index (RI) sensors are one of the most significant devices among the plasmonic devices because of their smaller size, and higher sensitivity [11]. These plasmonic RI sensors have various applications, they are used to detect different dielectric materials like gases, chemicals, biomolecules, viruses, cancer cells, etc. [12] with very high sensitivity.

In recent days, researchers are working on improving the sensitivity, resolution, quality factor, and figure of merit of the refractive index sensors.

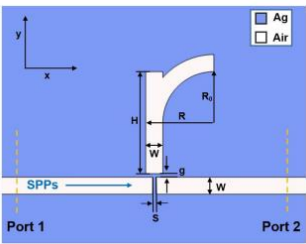
1.4 Literature Review:

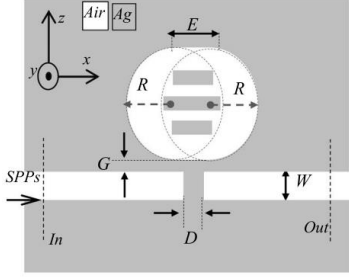
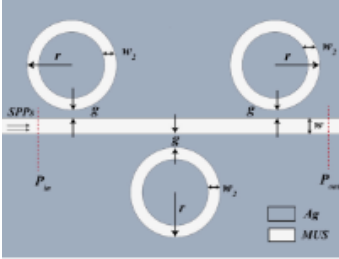
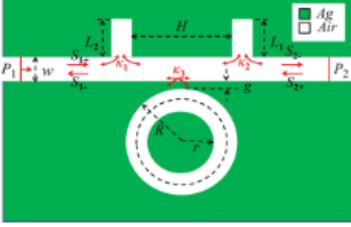
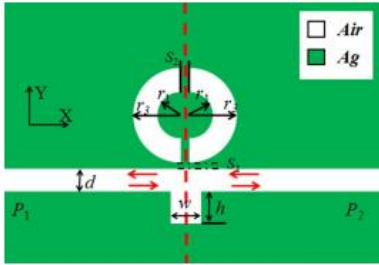
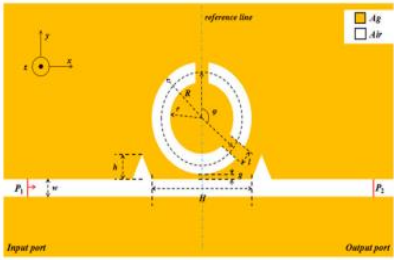
Since the late 1980s, surface plasmon-based sensors have become a great research topic for researchers. Sensitivity and Figure of Merit (FOM) play the most important roles in a plasmonic sensor's performance and quality.

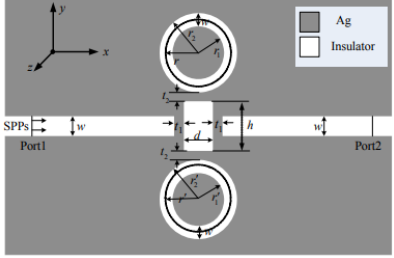
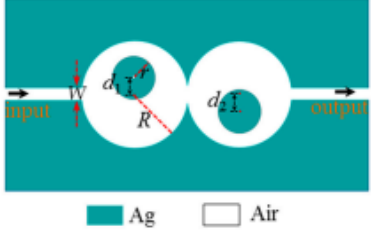
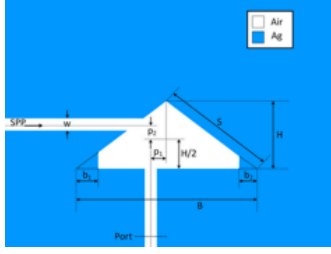
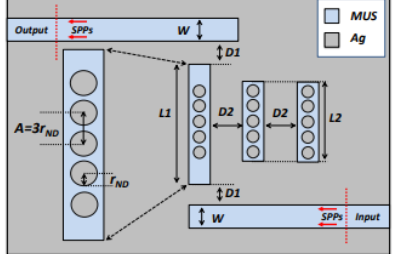
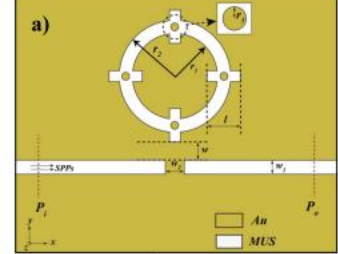
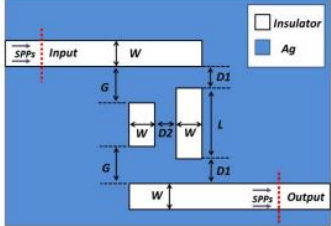
The sensitivity and FOM of a RI sensor show how accurately a sensor is able to detect changes in refractive index.

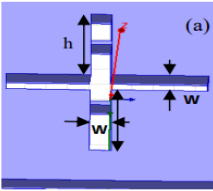
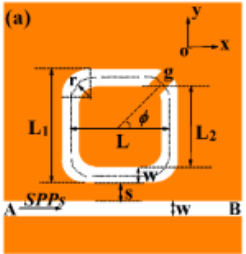
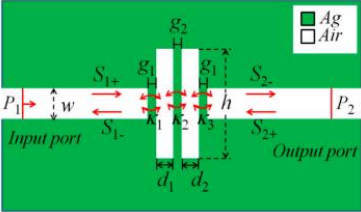
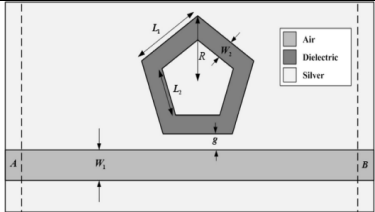
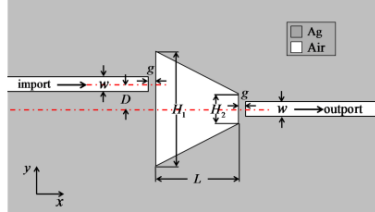
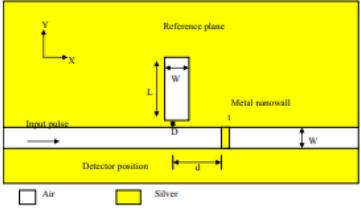
The researchers' goals are to enhance the sensors' FOM and sensitivity by suggesting various geometric shapes. **Table 1.1** show the comparison of different shapes resonators sensitivity and FOM of recent years.

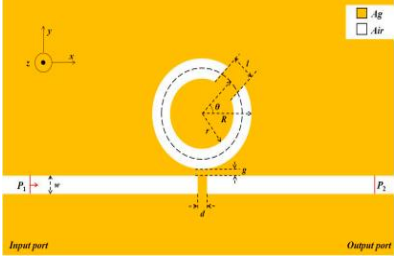
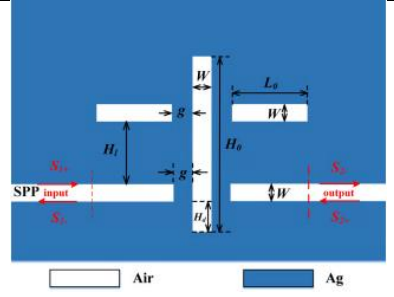
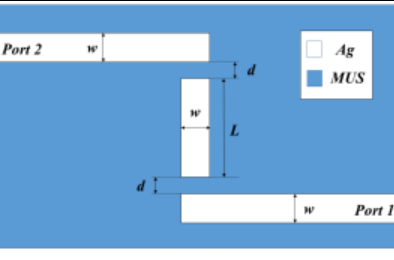
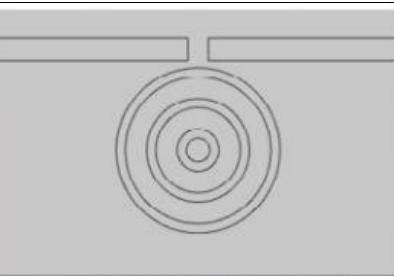
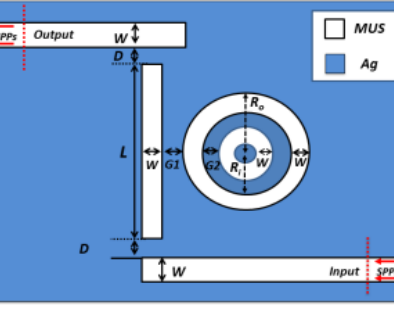
Table1.1: Comparison of different shapes resonators sensitivity and FOM

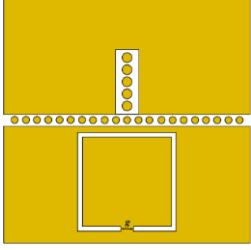
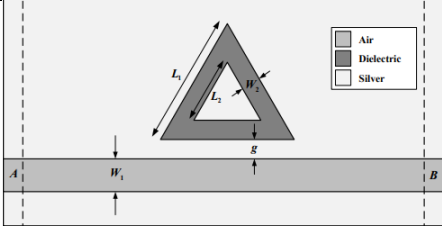
Structure Name	Sensitivity (nm/RIU)	FOM (RIU ⁻¹)	Figure	Ref.
r-shaped resonator	1333	5876		[13]

Defective oval resonator	2844.95	2.27 * 10E4		[14]
Multiple ring Resonator	3573.3	21.9		[15]
MIM waveguide with two stubs coupled with one ring resonator	1268	280		[16]
Tooth cavity-coupled ring	1200	122		[4]
Resonator with two triangle stubs coupled with a circular split-ring resonance cavity	1500	65.2		[17]

Dual side-coupled ring resonator	1160	62		[18]
Cascaded double asymmetric cavities		74.3		[19]
Asymmetric triangular shaped resonator	987	3.2×10^5		[20]
Resonator with three rectangular with nanodot cavity	7564	120		[21]
Cog Shaped Resonator	6227.6	6.52		[22]
Resonator with two unequal cavity	2625.87	26.04		[23]

Resonator with tooth-shaped stubs	1060	176.7		[24]
Square type split-ring resonator	1700	60.7		[25]
Resonator with Double Rectangular Cavities	596	7.5		[26]
Pentagonal Resonator	2325	159.6		[1]
MIM waveguide-coupled trapezoid cavity	750	65.2		[27]
Resonator with Side-coupled cavity	985	28.2		[28]

Circular Split Ring Resonator	1114.3	55.71		[29]
Resonator with end-coupled vertical cavity side-coupled by two horizontal cavities	1011	47.91		[30]
DMD (Dielectric Metal Dielectric) waveguide sensor	818			[31]
Triple Ring Resonator	3639.79	91.02		[32]
Concentric Double-Ring Resonator	1070			[5]

Square-shaped resonator with nano-dot inside the waveguide	1074.88	32.4		[33]
Ring-type Triangular Resonator	2713	52.36		[3]

1.5 Thesis Objective:

The main goal of this thesis work is to develop a refractive index sensor with a MIM configuration to enhance the sensitivity of the sensor, which can be used for various applications like glucose level detection, cancer cell detection, dengue virus detection, gas sensing, etc.

The objectives of this thesis are:

- To propose new structures for RI sensors with MIM configurations.
- To optimize the parameters of the sensors to get higher sensitivity.
- To get the application of the sensors in various fields like gas detection, biomarker detection etc.
- To enhance the quality of the sensor.

1.6 Thesis Layout:

Chapter 2 explains the Maxwell's equation and other consecutive equations. It includes Finite Integration Technique (FIT), Finite-Difference Time Domain (FDTD), Finite Element Method (FEM) etc. Mainly, this chapter shows the theoretical analysis of some basic concepts related to the thesis work.

Chapter 3 depicts the theoretical background of the thesis work. Plasmonic material modeling, the Lorentz-Drude model these basic concepts were discussed. Silver is used for modeling the RI sensor and so the plasmonic properties of silver are also mentioned here.

Chapter 4 deals with the modeling of the sensors and the enhancements of their parameters. The whole process of determination to get the best value of structural parameters for getting higher sensitivity is described here. The applications of the sensors in different refractive index ranges are also presented

Chapter 5 gives the conclusion of the thesis work where the optimal design has been determined based on the sensitivity of the refractive index sensors reported in the research work. Future study in this area has been explored with regard to its prospects.

Chapter 2

Wave Theory

2.1 Maxwell's Equation

Maxwell's equations explain the relationship that characterizes the fundamental electromagnetic quantity. The equations' differential or integral forms can be used to express them, which is the foundation for electromagnetic analysis. Maxwell's equations' differential version is used by the finite element method (FEM), which is represented in the time-varying fields as,

$$\nabla \times \mathbf{H} = \mathbf{J} + \partial \mathbf{D} / \partial t, \quad (2.1)$$

$$\nabla \times \mathbf{E} = - \partial \mathbf{B} / \partial t, \quad (2.2)$$

$$\nabla \cdot \mathbf{D} = \rho, \quad (2.3)$$

$$\nabla \cdot \mathbf{B} = 0, \quad (2.4)$$

where, \mathbf{E} = Electric field intensity,

\mathbf{D} = Electric flux density/ displacement,

\mathbf{H} = Magnetic field intensity,

\mathbf{B} = Magnetic flux density,

\mathbf{J} = Current density,

ρ = Electric charge density.

These equations are also called Gauss's, Faraday's, and Maxwell-Ampere's laws of the electric and magnetic forms, respectively. Another one is the continuity equation.

2.2 Constitutive equations

The constitutive equations, which describe the material's properties in contact with the fields, are crucial in understanding the creation of charge and current. The formulas for these equations are,

$$D = \epsilon_0 E + P, \quad (2.6)$$

$$B = \mu_0(H + M), \quad (2.7)$$

$$J = \sigma E, \quad (2.8)$$

The constitutive equation for linear materials, which have constant material properties with the variation of the applied field is given by,

$$B = \mu_0(1 + \chi_m)H = \mu_0\mu_r H = \mu H, \quad (2.9)$$

$$D = \epsilon_0(1 + \chi_e)E = \epsilon_0\epsilon_r E = \epsilon E, \quad (2.10)$$

The magnetization vector, M , which characterizes a material's magnetization due to a magnetic field (H), is similarly depicted as the volume density of the magnetic dipole moment. For the linear materials, this magnetization M is directly proportional to the magnetic field,

$$M = \mu_0\chi_m H \quad (2.11)$$

$$\text{Where, } \epsilon_r = (1 + \chi_e), \quad (2.12)$$

$$\mu_r = (1 + \chi_m) \quad (2.13)$$

Generalized Constitutive Equation

Some materials can exhibit non-zero polarization in the absence of an electric field. In more general situations, the constitutive equations for these non-linear materials can be written as

$$D = \epsilon_0 E + D_r,$$

where D_r stands for remanent electric flux density or the electric flux density in the absence of an electric field.

Similar to this, some materials can exhibit nonzero magnetization even in the absence of a magnetic field. The constitutive equations for these non-linear materials can be written as

$$\mathbf{B} = \mu_0 \mathbf{H} + \mathbf{B}_r, \quad (2.14)$$

where \mathbf{B}_r stands for remanent magnetic flux density or the magnetic flux density that exists without a magnetic field. Now, by including an externally generated current \mathbf{J}_e to the constitutive equation, the current density described in equation (2.8) can be generalized. The formula for this relationship is

$$\mathbf{J} = \nabla \times \mathbf{E} + \mathbf{J}_e \quad (2.15)$$

Wave

Equation:

Now, eqs. (2.1), (2.13), and (2.14) are evaluated, and the result is eq.

$$\nabla \times (\nabla \times \mathbf{E}) = -\mu_0 \nabla \times \mathbf{J}_e - \mu_0 \nabla \times \nabla \times \mathbf{E} \quad (2.16)$$

Additionally, this equation becomes when $\nabla \cdot \mathbf{J}_e = 0$, and $\nabla \cdot \mathbf{E} = 0$ are considered.

2.3 Finite-Difference Time Domain (FDTD)

The Yee algorithm is used in the finite-difference time-domain (FDTD) to solve EM wave problems. In order to loop around a magnetic field component with an electric field and vice versa, the user must sequentially update the electric and magnetic field values from the computational grid.

With such a plan, the complexity of curl rotations in Maxwell's equations is greatly reduced. In addition, updating the related equations only requires the values of neighboring cells, making parallelization easier. In summary, the basic two-step FDTD computing procedure is as follows:

1. Updating the electric field components from the previous iteration's magnetic field components, and 2. updating the electric field components of the prior iteration's magnetic field components.
2. Equations (2.1) and (2.2) form the foundation of the FDTD approach. The fields are vectors in three dimensions. Each equation can be multiplied by three to create three connected scalar first-order differential equations with time- and space-dependent derivatives.

2.4 Finite Integration Technique (FIT)

The original formulation of the finite integration technique (FIT) was made by Weiland et al. [34]. The integral forms of Maxwell's equations (2.1) through (2.4) are the focus of FIT. Additionally, the method uses every vector component of the E and H-field situated in a double-grid system. Weiland [35] eventually transformed the FIT equations into a matrix format, enabling the use of irregular and non-orthogonal grids for computing. Additionally, FIT has the advantage of using less computational memory than FDTD [36]. The computational domain of FIT is proposed to be formulated as a one-dimensional staggered grid. Assume the grid's range is $[0, K]$, where x_n is a finite sequence of n grid points and $0 = x_0 < x_1 < \dots$. Let $x_i = i K/n$, $i = 0, \dots, m$ be the uniform grid with a mesh size of $S = K/n$ for a uniform 1D grid. Since $i = 1, \dots, m$, the corresponding staggered grid is $s_i = (i - 1/2) K/n$.

2.5 Finite Element Method (FEM)

To represent the phenomena of fluid dynamics, electromagnetics, and thermal analysis, partial differential equations (PDEs) are typically used. However, these phenomena involve complex geometries and inhomogeneous media. As a result, the PDEs' analytical solutions grow complicated. The finite element method (FEM) can be used to solve these problems more effectively. Compared to traditional, simpler-to-code techniques like FDTD and Method of Moments (MoM), the FEM can design EM wave problems with accurate material interface, rapid convergence, adaptive meshing, and high numerical resolution. The FEM pseudo-code can be created for a specific area of interest and applied to additional areas with little to no change [C. S. Desai and J. F. Abel, Introduction to the finite element method; a numerical method for engineering analysis. Van Nostrand Reinhold, 1971.]. The four steps for applying the FEM to examine any situation are [M. N. Sadiku, Numerical techniques in electromagnetics with MATLAB. CRC press, 2018.]:

The steps include:

1. Discretizing the computing domain into a finite number of elements,
2. determining the governing equations for a specific element,
3. Putting everything in place in the solution region.

4. Fix the equations that were created.

It is possible to write a generalized wave equation as

$$\nabla^2 \psi + k^2 \psi = g, \tag{2.17}$$

where g is the source and k is the waves.

Chapter 3

Plasmonic Materials

3.1 Refractive Index and Complex Permittivity

Dielectric permittivity, ϵ and magnetic permeability, μ are two variables that can be used to define the plasmonic properties of materials, which are mostly employed for their capacity to interact with light [37]. However, the permeability value approaches unity at optical wavelengths. Consequently, only the dielectric permittivity may completely describe their behavior.

A complex parameter, the metal's dielectric permittivity has a real part (ϵ_1) and an imaginary part (ϵ_2). The optical loss is caused by the imaginary part, whereas the actual part determines how the material responds to polarization. One of the most significant plasmonic features of metals is the real component of its negative dielectric permittivity at optical frequencies[38] When a material interacts with light, the presence of a negative real component in its permittivity plays a crucial role in generating Surface Plasmon Polaritons (SPPs) and facilitating their propagation at the material's interface. Consequently, for a material to be effectively employed in plasmonic devices, it is essential for its complex permittivity to possess a negative real component.

The negative real component of the permittivity enables the material to support the excitation and sustained propagation of SPPs. SPPs are collective oscillations of electrons at the interface between a metal and a dielectric material, resulting from the coupling between incident light and free electrons in the metal. The negative real component of the permittivity allows for the resonance condition necessary for the excitation of SPPs to be met, leading to their creation and subsequent propagation along the interface.

In plasmonic devices, SPPs are exploited for their unique properties, such as strong confinement and subwavelength localization of electromagnetic energy. These properties enable the manipulation and control of light at the nanoscale, offering opportunities for applications such as sensing, imaging, and integrated optics.

Therefore, in the context of plasmonic devices, materials with a negative real component of the complex permittivity are highly desirable. This characteristic allows for efficient excitation and

propagation of SPPs, which in turn enables the realization of various functionalities and performance enhancements in plasmonic devices.

In summary, the negative real component of the complex permittivity in a material is instrumental in the generation and propagation of SPPs. This property is crucial for the effective utilization of the material in plasmonic devices, enabling advancements in nanophotonics and the development of innovative technologies.

3.2 Plasmonic Material Modeling

At low frequencies or for long wavelengths, metals make ideal conductors. They have no field; hence they are not dispersive in nature. Metals, however, display a dispersive character at optical wavelengths. Metals act as dielectrics at frequencies above the optical frequency range. Three vectors can be used to predict how a material will behave when exposed to an external scillating electromagnetic field. They are E (electric field intensity), P (polarization density), and D (electrical flux density). They are given as,

$$D(\omega) = \varepsilon(\omega) E(\omega) , \quad (3.1)$$

$$P(\omega) = \varepsilon_0 \chi(\omega) E(\omega) , \quad (3.2)$$

$$D(\omega) = \varepsilon_0 E(\omega) + P(\omega) , \quad (3.3)$$

Combining equations 3.2 and 3.3 we get,

$$D(\omega) = \varepsilon_0 E(\omega) (1 + \chi(\omega)) \quad (3.4)$$

The electric susceptibility can be shown here. The susceptibility is a dimensionless quantity that expresses how quickly a material becomes polarized in response to an applied electric field.

Now, comparing equation 3.1 and 3.4, the relation between permittivity and susceptibility stands as,

$$\varepsilon(\omega) = \varepsilon_0 (1 + \chi(\omega)), \quad (3.5)$$

Therefore, the relative permittivity is given by,

$$\varepsilon_r(\omega) = 1 + \chi(\omega). \quad (3.6)$$

In the case of a dispersive material, the frequency dependent permittivity and susceptibility should be accurately modeled in order to determine the material's ideal response to a certain electromagnetic excitation, even though the aforementioned values become straightforward for linear isotropic materials like glass. To mathematically address this reliance, the Drude model, Lorentz model, and Lorentz-Drude model are frequently utilized.

3.3 Drude Model

The complex dielectric permittivity of plasmonic metals like gold and silver can be given by the Drude model [11].

$$\varepsilon_D(\omega) = \varepsilon_\infty - \frac{\omega_D^2}{\omega(\omega + i\gamma_D)} \quad (3.7)$$

Here,

ω_D is the bulk plasma frequency,

γ_D is the intraband damping term (inverse of the relaxation time, τ),

ε_∞ is the relative permittivity for high frequencies,

And i is the imaginary unit. ω_D is to be calculated using this formula,

$$\omega_D = \sqrt{\frac{N_e q^2}{\varepsilon_0 m_0}} \quad (3.8)$$

3.4 The Drude-Lorentz model

Two scientists named Drude and Lorentz presented a theory model for the complicated index of refraction and dielectric constant of materials (around 1900). The concept is based on the use of

particles resembling electrons that are harmonically bound to external electrical fields. The Drude-Lorentz model, which is used to define the dielectric constant of gold, is given in equation (3.9).

s. Drude-Lorentz model separates free-electron effects and bound-electron effects on complex dielectric function [39][40]. To obtain the dielectric constant of gold, it is defined by the DrudeLorentz model which is expressed in equation (3.9).

$$n_g^2 = \varepsilon_\infty - \frac{w_D^2}{w(w+j\gamma_D)} + \frac{\Delta\varepsilon^2\rho}{(w^2 - \rho^2) + j\tau w} \quad (3.9)$$

3.5 Plasmonic Properties of Silver

The The values of different parameters of (2.1) and (2.3) for silver are obtained by Barchiesi et al. [41] and given in Table 3.1.

Table3.1: Different parameters of Drude model and Lorentz-Drude model and their values for silver.

Parameters	Value
ε_∞	0.114773
ω_D	$1.32589 \times 10^{16} \text{ rad/s}$
γ_D	$7.05499 \times 10^{15} \text{ rad/s}$
$\Delta\varepsilon$	3.62762
ω_L	$41.58116 \times 10^{16} \text{ rad/s}$
γ_L	$1.04632 \times 10^{14} \text{ rad/s}$

The complex permittivity of gold can be calculated using equations (3.7) and (3.8) and by referring to the values provided in Table 2.1. These equations allow us to determine both the real and imaginary parts of the permittivity at different wavelengths for both the Drude model and the

Lorentz-Drude model. By plotting these values, we can visualize the behavior of gold's permittivity as a function of wavelength and gain a deeper understanding of its optical properties.

To elaborate further, the Drude model describes the permittivity of a material based on the collective response of free electrons to an applied electric field. On the other hand, the Lorentz-Drude model incorporates additional contributions from bound electrons in the material.

By obtaining the values from Table 2.1, which provides the necessary parameters for these models, we can calculate the real and imaginary parts of the complex permittivity for different wavelengths. These calculations allow us to examine how the permittivity of gold varies with the incident light's wavelength.

Visualizing this data through plots helps us analyze and interpret the optical behavior of gold. The plots can reveal important features, such as resonances, absorption peaks, and dispersion characteristics. By understanding the complex permittivity of gold at different wavelengths, we can gain insights into its interaction with electromagnetic waves and its applications in various fields, such as plasmonics, nanophotonics, and optoelectronics.

In summary, through the utilization of equations (3.7) and (3.8) and the information provided in Table 2.1, we can calculate and plot the real and imaginary parts of gold's complex permittivity for different wavelengths using the Drude and Lorentz-Drude models. These plots enable us to visualize and analyze the optical properties of gold, contributing to our understanding of its behavior in electromagnetic wave interactions.

3.6 Performance Matrix: Sensitivity

Sensitivity is the most important performance factor for a RI sensor. The following equation [42] can be used to determine sensitivity (S) from a change in resonance wavelength location and the associated change in refractive index.

$$S = \frac{\Delta\lambda}{\Delta\eta} \quad (3.10)$$

where, $\Delta\lambda$ = change in resonant wavelength, and $\Delta\eta$ = change in refractive index.

Both redshift and blueshift are possible manifestations of the shift in resonance wavelength. In Fig. 3.1, the green curve is blueshifted, while the pink curve is redshifted. S can be computed by finding the difference between the corresponding η and λ .

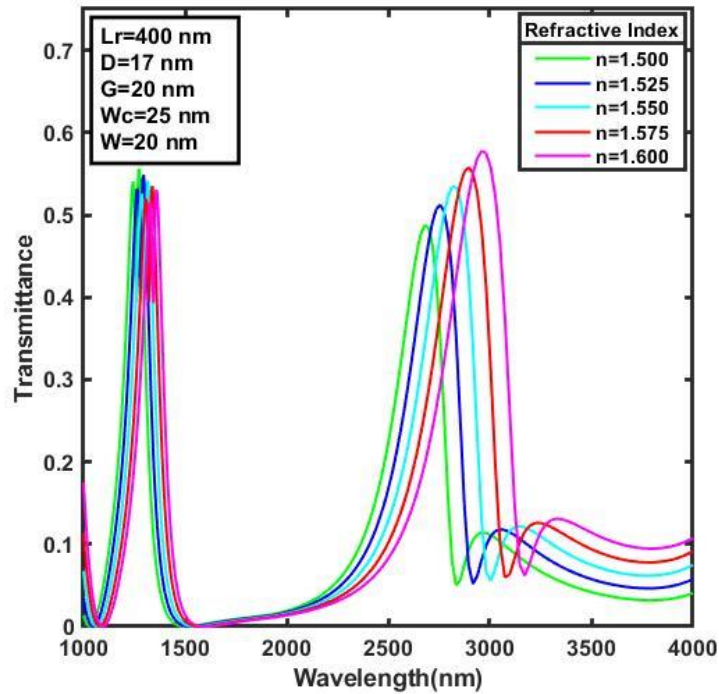


Figure 3.1. Sensitivity

Chapter 4

Re-simulation of Existing Papers

4.1 Re-Simulation with COMSOL Multiphysics

To ensure adequate simulation setup for the suggested devices, it is crucial to resimulate several published works. Three of these papers are reevaluated in this section using the for-profit EM program COMSOL Multiphysics.

By simulating these papers, we can verify our methodology, assess the software's capabilities, and establish benchmarks for future device design. COMSOL Multiphysics offers comprehensive electromagnetic simulation tools, making it suitable for this purpose.

4.2 Concentric Triple Ring Resonator

The paper is titled as “*A highly sensitive plasmonic refractive index sensor based on concentric triple ring resonator for cancer biomarker and chemical concentration Detection*” [32] this work, to maximize the sensitivity of the developed sensor, the basic structural parameters are optimized one at a time. As a result, the maximal sensitivity for gas sensing is 3639.79 nm/RIU, with corresponding FOM (Figure of Merit), FOM*, and Q-factor values of 91.02, 0.26 106, and 99.75. The suggested enhanced CTRR sensor may also be used as a plasmonic filter and has a maximum sensitivity of 7530.49 nm/RIU for the physiologically and chemically significant refractive index range of 1.30 to 1.40. The proposed sensor is a strong contender in the field of refractive index sensing as a result of the many potential applications.

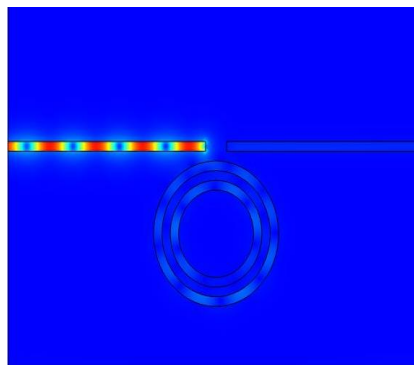


Figure 4.1 Power transmission characteristic of the designed structure

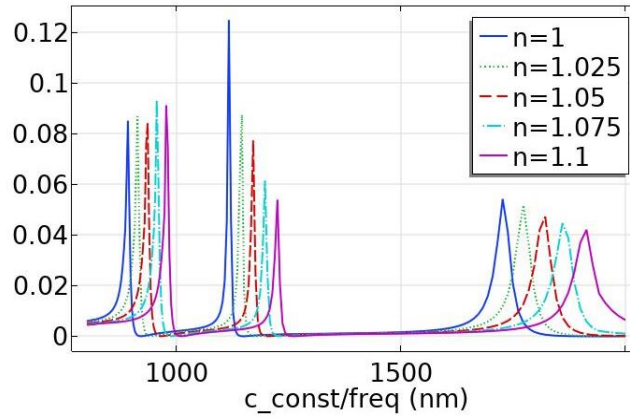


Figure 4.2 Transmittance spectrum for different refractive indices

4.3 Ring-Type Pentagonal Resonator

The title of this existing work is “*Plasmonic Refractive Index Sensor Based on Ring-Type Pentagonal Resonator with High Sensitivity*” [1] The sensor is made up of a straight waveguide attached to a standard pentagonal ring resonator. The highest sensitivity recorded has a figure of merit of 46 and is as high as 2325 nm/RIU. The sensor's dielectrics with refractive indices between 1 and 1.02 and 1.34 and 1.40 have been examined.

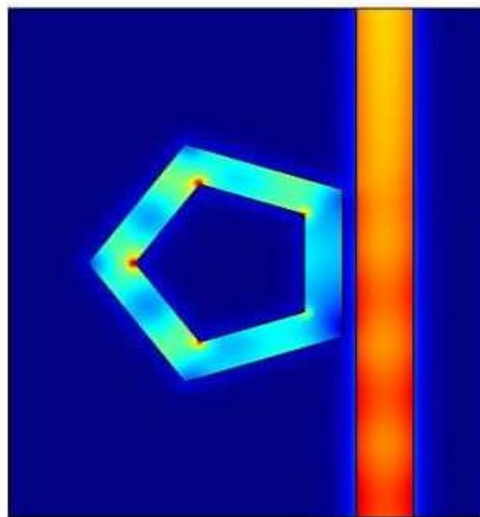


Figure 4.3 Power transmission characteristic of the designed structure

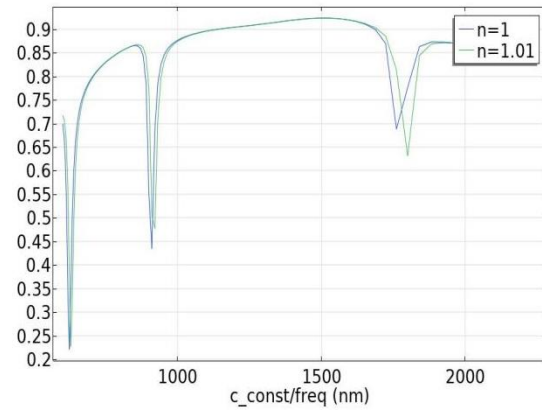


Figure 4.4 Transmittance spectrum for different refractive indices

Chapter 5

Plasmonic Sensor Design and Performance Analysis

Over time, optical devices transitioned from GHz speeds and μm dimensions to smaller components in the nanometer range, while maintaining the same operating speed. However, heat loss and time delays posed limitations. To meet the demand for high-speed optical systems, dielectric photonics emerged, offering PHz speeds and μm -sized devices. However, the bulky size of dielectric photonics hindered dense packaging due to the diffraction limit. To address this, Surface Plasmon Polaritons (SPPs) were introduced, bridging the gap between dielectric photonics and semiconductor technologies, enabling chip-scale integration of optical devices.[7]

At the junction where a metal and a dielectric material meet, an intriguing phenomenon called Surface Plasmon Polaritons (SPPs) occurs. These SPPs are electromagnetic waves that propagate along this interface. They are formed due to the interaction between two distinct entities: surface plasmons, which arise from the oscillations of electrons on the metal surface, and polaritons, which are associated with the electromagnetic fields on the dielectric surface [1], [3]

Characterized by an exponentially decaying profile in the perpendicular direction [4] and with the ability to modulate light in the deep subwavelength range, SPPs have shown the potential to overcome the diffraction limit of light [1], [5], [6]. Therefore, SPPs have been implemented to make highly integrated optical devices like refractive index sensors [1], [3]–[5], [7]–[9], demultiplexers [6], biosensors [1], and filters [10].

5.1 Refractive Index Sensors

Refractive index (RI) sensors based on Surface Plasmon Polaritons (SPPs) are widely adopted in research due to their simplicity and effectiveness. These sensors utilize the shift in resonant wavelength to detect and identify unknown materials. A considerable number of RI sensors have been reported to date, employing diverse types of waveguides for their operation [7].

Refractive index sensors are primarily designed to detect changes in the refractive index of the material being sensed. Plasmonic refractive index sensors commonly utilize various resonator structures such as rings, gratings, octagons, rectangles, and more, to achieve a resonance peak in

the transmission characteristics. The resonant peak undergoes a shift as the refractive index of the sensed material changes. The sensitivity of the sensor can be determined by calculating the resonance shift using the formula:

$$S = \Delta\lambda / \Delta n \quad (5.1)$$

where, S is the sensitivity, $\Delta\lambda$ is the resonant wavelength shift and Δn is the change in refractive index

For effective detection of even minute changes in the refractive index, the sensor should ideally possess a high sensitivity (S) while minimizing the change in refractive index (Δn).

5.2 Refractive Index Sensor with MIM Waveguide

Recently, MIM structures have been highly considered as compact plasmonic waveguide structures because of their appreciable propagation lengths, ease of fabrication, and the potential to generate strong field confinement [3], [5], [7]. MIM structured waveguide can be used to transmit optical and electrical signals, embedding conventional electronic and photonic circuits on the same chip structure [1], [3]. Refractive index (RI) sensors are one of the most researched arenas for their multipurpose and dynamic applications, e.g., temperature sensing [43], glucose sensing [5], gas sensing [44], biological [45], [46], and chemical sensing [20].

5.3 Our Proposed Structure with Semi-Circular Cavity

5.3.1 Basic Structure

The two-dimensional schematic of the proposed plasmonic sensor is comprised of input and output MIM waveguides which are coupled with a Semicircle-shaped resonator. The input port is positioned to the left and the output port is positioned to the right of the MIM waveguide. In Figure.5.1, the blue shaded area represents the silver (Ag) and, the white shaded zone represents the material under sensing (MUS). As silver metal has lower Drude damping, it shows better performance in sensitivity and detectability than gold (Au).

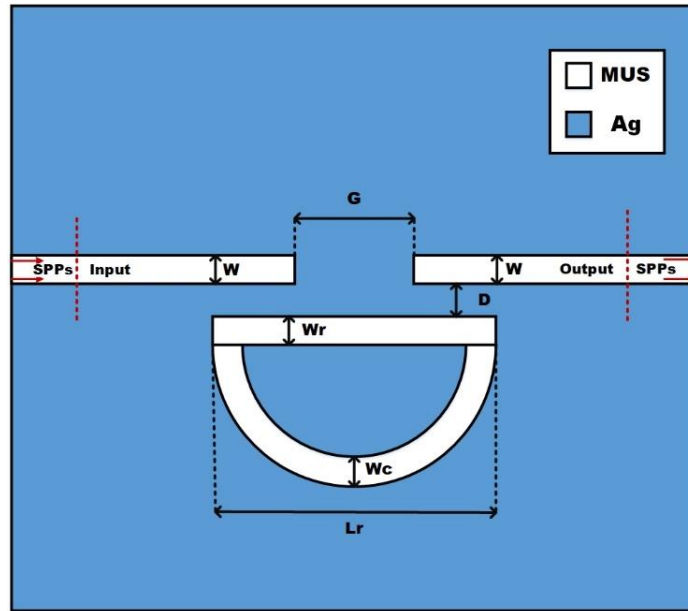


Figure 5.1 Two-dimensional (2D) schematic of the proposed RI sensor 1

The initial structural parameters of the proposed refractive index (RI) nanosensor are presented in Table 5.1. The distance between the waveguide and resonator is denoted by D and has a value of 17 nm. The diameter of the semicircle is represented by L_r and measures 400 nm. The width of the rectangular cavity is denoted as W_r and is 25 nm wide. The semi-circular cavity has a width denoted by W_c , which also measures 25 nm. The waveguide has a width denoted by W , which is 20 nm wide. Additionally, there is a baffle with a width denoted by G , which is 20 nm wide.

5.3.2 Initial Results

The proposed work is modeled using the finite element method (FEM) in COMSOL Multiphysics 5.3, and all calculations are performed in MATLAB. Electromagnetic Waves Frequency Domain (ewfd) is used as the physics interface. Scattering boundary conditions (SBC) are applied to absorb the evanescent EM-field energy with very little reflection. Extra-fine triangular mesh is utilized for discretization.

Table 5.1 Initial structural Parameters of the sensor

Parameters	Symbols	Values(nm)
Distance between waveguide and resonator	D	17
The diameter of the semicircle	Lr	400
Width of the rectangular cavity	Wr	25
Width of the semi-circular cavity	Wc	25
Width of the waveguide	W	20
Baffle	G	20

Resonant wavelength is the wavelength at which the transmittance peaks are established. With the change in refractive index or any of the perceptual dimensions of the RI sensor variation, the resonant wavelengths get shifted to the longer or shorter wavelength region, which leads to the identification of the unknown material. This is a critical concept for an RI sensor.

Keeping the MUS refractive index fixed at 1.55, the following four structural parameters, G, D, Lr, and Wc, were initially specified at 20 nm, 17 nm, 400 nm, and 25 nm, respectively. The transmittance peaks obtained for the initial parameters at 1283 nm twinned with another peak at 1317 nm for peak-I and 2824 nm for peak-II are depicted in Figure 5.2.

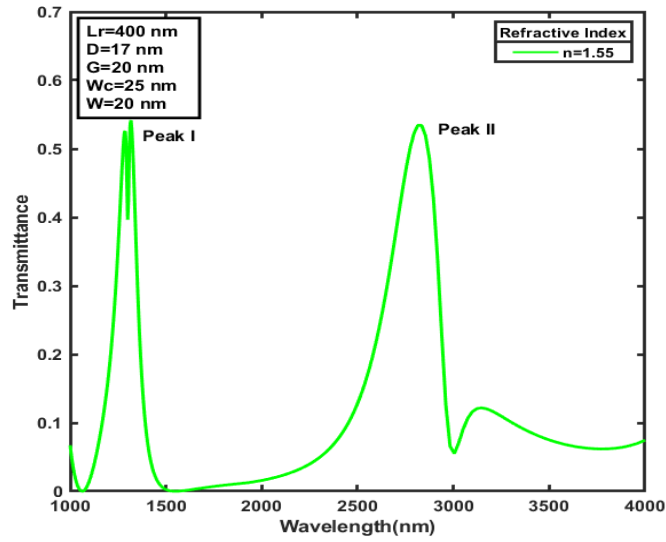


Figure 5.2 The transmittance peaks obtained for the initial parameters at 1283 nm twinned with another peak at 1317 nm for peak-I and 2824 nm for peak-II

To study the change of refractive index on the spectrum, it was altered from 1.5–1.6 with a 0.025 step size. Both the transmittance peaks undergo a redshift with the increasing value of the refractive index. Figure.4.3 shows the transmittance response for different values of n

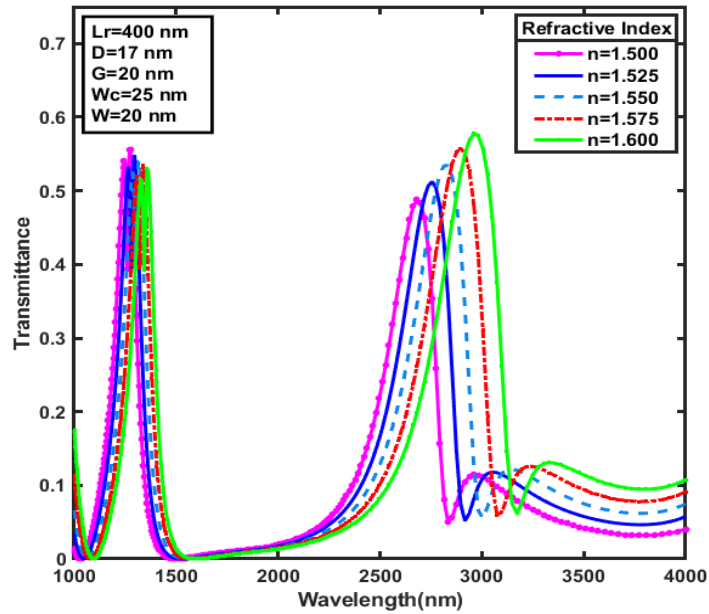


Figure 5.3 Variation of refractive index, n , on the initial transmittance profile

Figure 5.4 illustrates the field distribution pattern for different resonant and non-resonant frequencies.

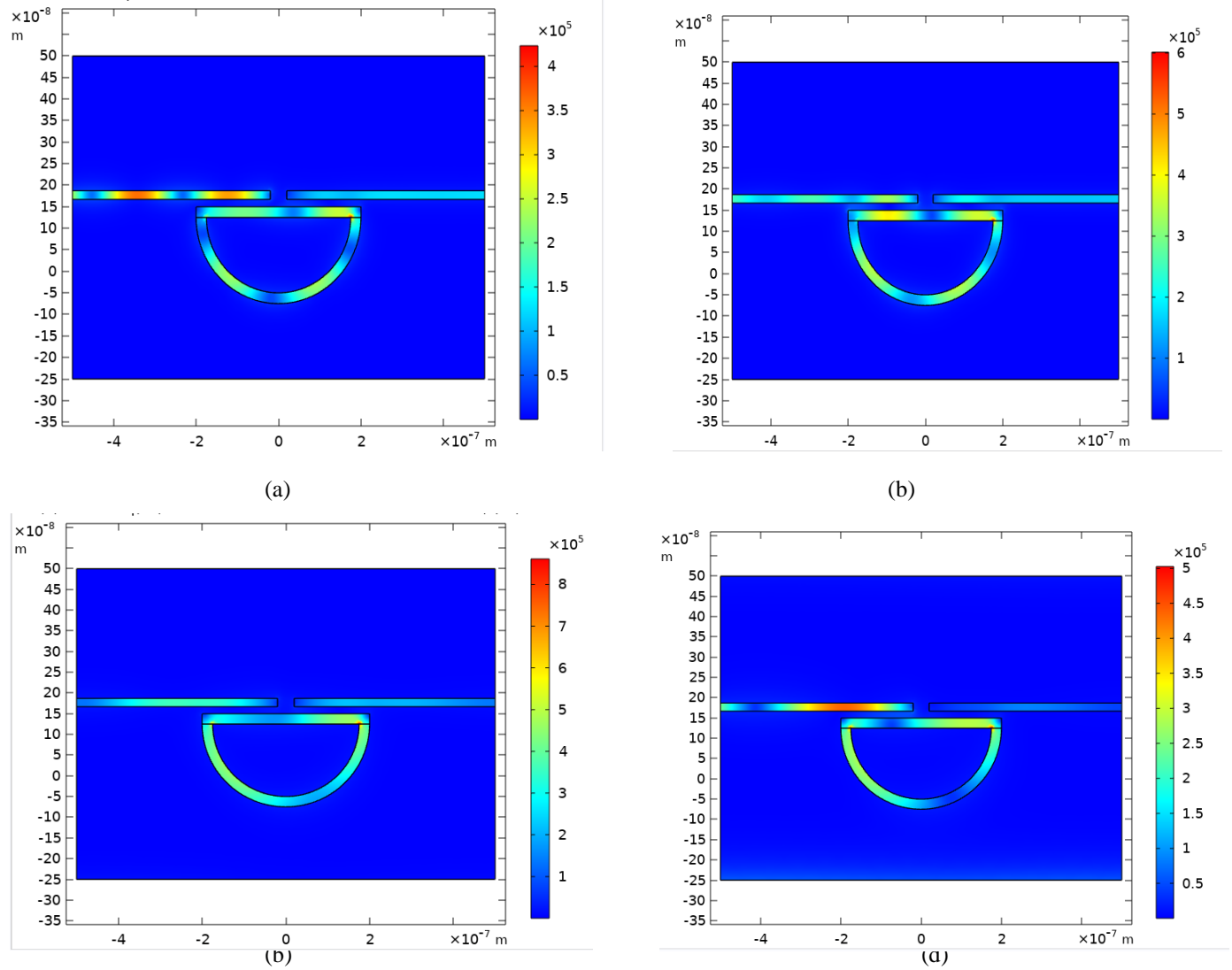


Figure 5.4 Normalized Electric Field (V/m) at frequencies (a) 1283 nm, (b) 1317 nm, (c) 2824 nm and, (d) 3637 for the initial structure.

5.3.3 Optimization of Initial Parameters

Keeping the MUS refractive index fixed at 1.55, the following four structural parameters, G , D , L_r , and W_c , were initially specified at 20 nm, 17 nm, 400 nm, and 25 nm, respectively. The transmittance peaks obtained for the initial parameters at 1283 nm twinned with another peak at 1317 nm for peak-I and 2824 nm for peak-II are depicted in Figure 5.2. To study the change of

refractive index on the spectrum, it was altered from 1.5–1.6 with a 0.025 step size. Both the transmittance peaks undergo a redshift with the increasing value of the refractive index. Figure 5.3 shows the transmittance response for different values of n . G , D , L_r and, W_c are then altered separately without adjusting the values of the other parameters.

The cavity length of the semi-circle’s rectangular part, L_r is varied from 400 nm to 440 nm with an increment of 10 nm. The resonant wavelength undergoes redshift with increasing values of L_r , which is depicted in Figure 5.5.

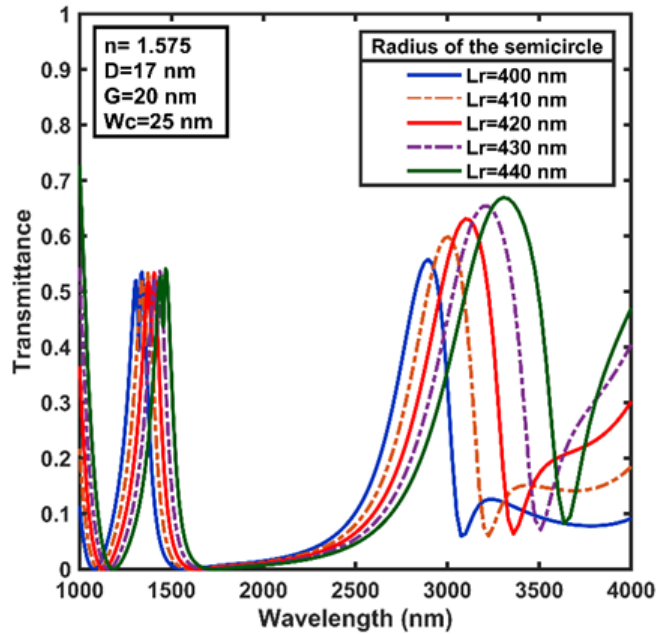


Figure 5.5 Transmittance spectrum for different length of the cavity, L_r

The width of the waveguide, W_c , is next adjusted between 25-29 nm with a 1 nm increment, and the consequential plot in Figure 5.6 represents the resonant wavelength showing the increment, i.e., blue shift for the increment of the width of the waveguide.

The distance between the waveguide and the resonator, D , is then altered between 17–20 nm with a 1 nm increment, and the resulting plot in Figure 5.7 illustrates resonant peaks shift towards more significant, i.e., red shift of the wavelengths.

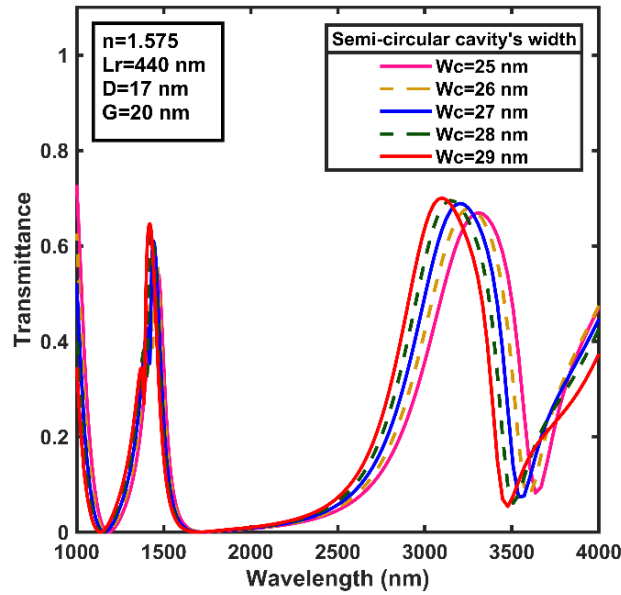


Figure 5.6 Transmittance spectrum for different width of the semi-circle, W_c .

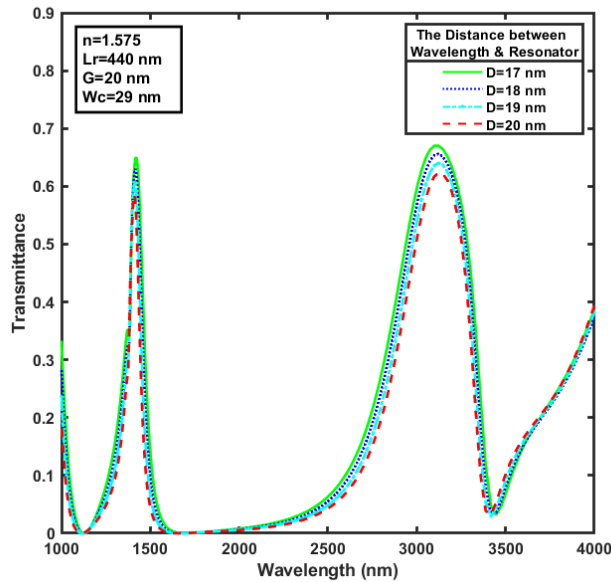


Figure 5.7 Transmittance spectrum for different distance between wavelength and resonator, D

Correspondingly, the transmittance of the sensor with the resonator for different values of the gap, G , is represented in Figure 5.8, where G was varied from 20 nm to 25 nm with an interval of 1 nm. The resonance wavelength is shifting to the left, i.e., decreasing with the enlargement in the gap, G . The optimized value for which the highest performance was observed was 25 nm.

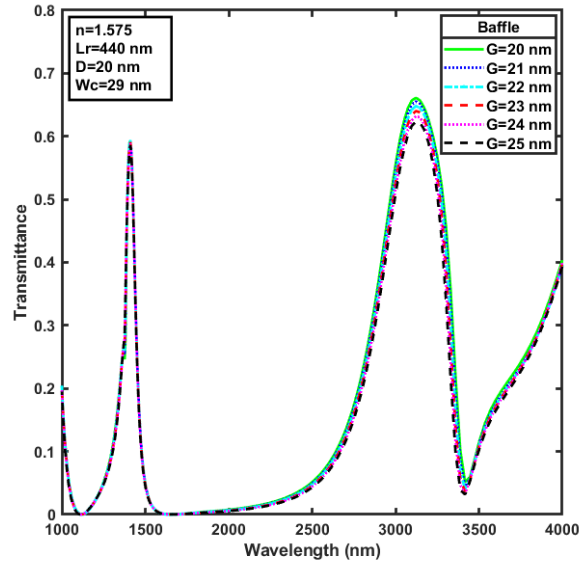


Figure 5.8 Transmittance spectrum for different baffle, G

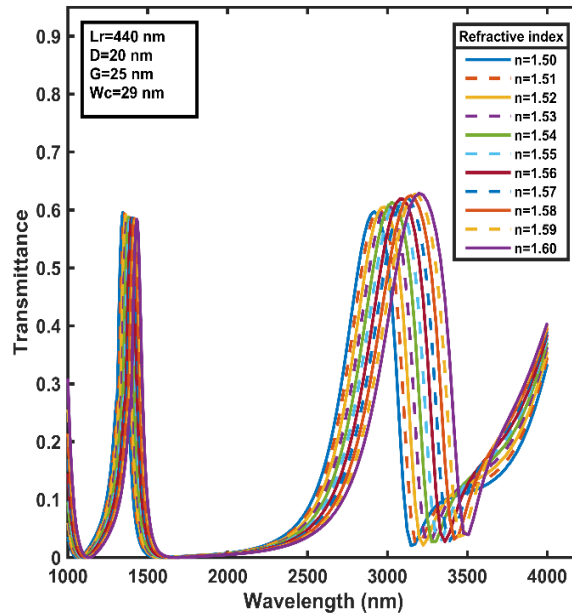


Figure 5.9 Transmittance spectrum for different refractive indices with the most optimized structural parameters.

In order to get the highest sensitivity, G, D, Lr, and Wc values are adjusted to 25 nm, 20 nm, 440 nm, and 29 nm, respectively, after thorough simulations. The transmission spectrum of the demonstrated sensor is once more simulated using the updated structural parameters by varying the MUS's refractive index in steps of 0.01 between 1.5 and 1.6. The transmission spectra in Figure 5.9 were used to figure out the variations in the resonant wavelengths for the two peaks.

Peak-II has a sensitivity of 4859 nm/RIU, which is the highest. Consequently, is the best choice for sensing activities.

Table 5.2 summarizes the structural parameters of the proposed sensing device that extract the most acceptable achievable consequence in terms of the refractive index.

Table 5.2 Optimized structural Parameters of the sensor

Parameters	Symbols	Values(nm)
Distance between waveguide and resonator	D	20
Diameter of the semicircle	Lr	440
Width of the rectangular cavity	Wr	25
Width of the semi-circular cavity	Wc	29
Width of the waveguide	W	20
Baffle	G	25

5.3.4 Application

Refraction index (RI) sensors have gained significant attention in various research fields due to their versatile and dynamic applications. These sensors have been extensively studied for their potential in diverse areas such as temperature sensing [43], glucose sensing [5], gas sensing [44], biological sensing [45]–[47] [48]–[50], optoelectronics [51]and chemical sensing [20], [52][14], pathological sensing [53] filter. Their ability to accurately measure and monitor these parameters has opened up new avenues for scientific advancements and practical applications. Researchers have focused on enhancing the sensitivity, selectivity, and reliability of RI sensors to enable their integration into a wide range of industries and disciplines.

5.3.4.1 Application as a glucose Sensor

The Refractive index of tissue varies with the change in its physical and chemical features [54]. It is well-known that glucose serves as the primary fuel for our brain and body cells, fulfilling most of our energy requirements. Hence, considering its vitality in the human body, proper glucose level monitoring is crucial. The device that detects glucose concentration in the human blood sample is called a glucometer. In a glucose solution, the refractive index increases linearly with changes in concentration[55] The following formula is used to find the refractive index for differently concentrated glucose solutions [54]

$$n = 0.2015 \times C + 1.3292 \quad (4.2)$$

Here, n stands for the refractive index and C for the percentage of glucose content.

C is varied from 0% to 10% having an interval of 2%, and the corresponding refractive indexes have been computed using 5.2. Resonant transmission peaks undergo a redshift towards the larger wavelength, as illustrated in Figure 5.10. As a result, it was possible to detect the changes in low glucose concentration levels. Again, for monitoring more significant variation in the concentration, C was again varied from 0% to 30%. This time step size of 10% was selected. Figure 5.11 displays the effect of varying C on the transmission spectrum of peak-II of the proposed sensor.

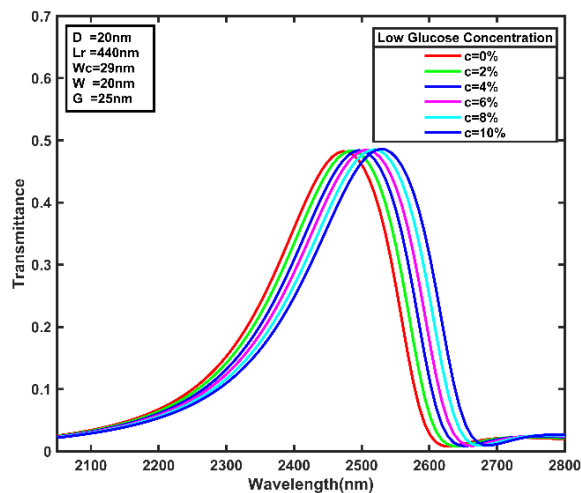


Figure 5.10 Transmittance spectrum for different values of low glucose concentration

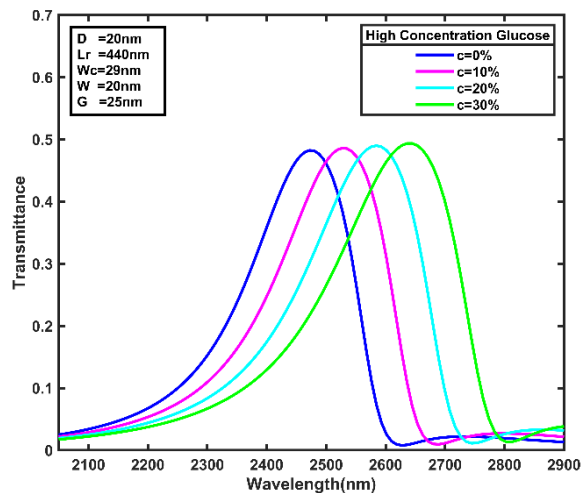


Figure 5.11 Transmittance spectrum for different values of high glucose concentration

Table 5.3 and 5.4 list the glucose concentration in percentage, the respective refractive index values, and the corresponding sensitivity.

Table 5.3 Sensitivity Analysis for Different Values of Low Glucose Concentration

Glucose concentration, C (%)	Refractive index, (n)	Sensitivity(nm/RIU)
0%	1.3292	----
2%	1.3332	3863
4%	1.3376	1772
6%	1.3413	4255
8%	1.3453	1986
10%	1.3493	1999

Table 5.4 Sensitivity Analysis for Different Values of High Glucose Concentration

Glucose concentration, C (%)	Refractive index, (n)	Sensitivity(nm/RIU)
0%	1.3292	----
10%	1.3493	2733
20%	1.3695	1305
30%	1.3896	1624

Therefore, the reported sensor is expected to serve as a potential glucose sensor on the merit of its capacity to detect a small as well as large concentration of glucose solution. The tabular analysis illustrates that the proposed sensor offers a maximum sensitivity as high of 4255 nm/RIU and 2733 nm/RIU for lower and higher concentrated glucose solutions respectively.

5.3.4.2 Application as a Cancer Biomarker

The proposed optimized refractive index (RI) sensor exhibits exceptional sensitivity, making it suitable for early-stage detection of cancer biomarkers. An important biomarker related to cancer is the abnormal refractive index value of the cytoplasm within cells. While healthy cells typically have a cytoplasm with an RI of 1.36, cancerous cytoplasm falls within the range of 1.38 to 1.401, indicating the presence of excessive proteins [56]–[58].

Given that cancer cells are usually in the micrometer range [57], it is not feasible to insert an entire cell into the cancer detection sensor known as CTRR. However, by utilizing standard centrifugation techniques, specific cell components like the nucleus and cytoplasm can be isolated. The extracted cytoplasmic fluid can then be applied to the cavities and waveguide-cores of the nanosensor for cancer detection. Figure 14 illustrates the transmittance spectra of a normal cell

and three different types of cancer cells, focusing on the most sensitive peak of the optimized model. The distinct peaks displayed in Figure 5.12 enable the designed structure to accurately differentiate between healthy and cancer cells. Table 3 provides sensitivity values for each cancerous sample, showcasing the potential of the proposed design as a cancer cell detector.

Table 5.5: Performance of the optimized sensor as a cancer biomarker [56]–[58]

Cell	Affected Area	Refractive Index	Sensitivity(nm/RIU)
Normal	-----	1.360	-----
Basal	Skin	1.380	2517
MDA MB-231	Breast	1.399	2510
Jurkat	Blood	1.390	1879

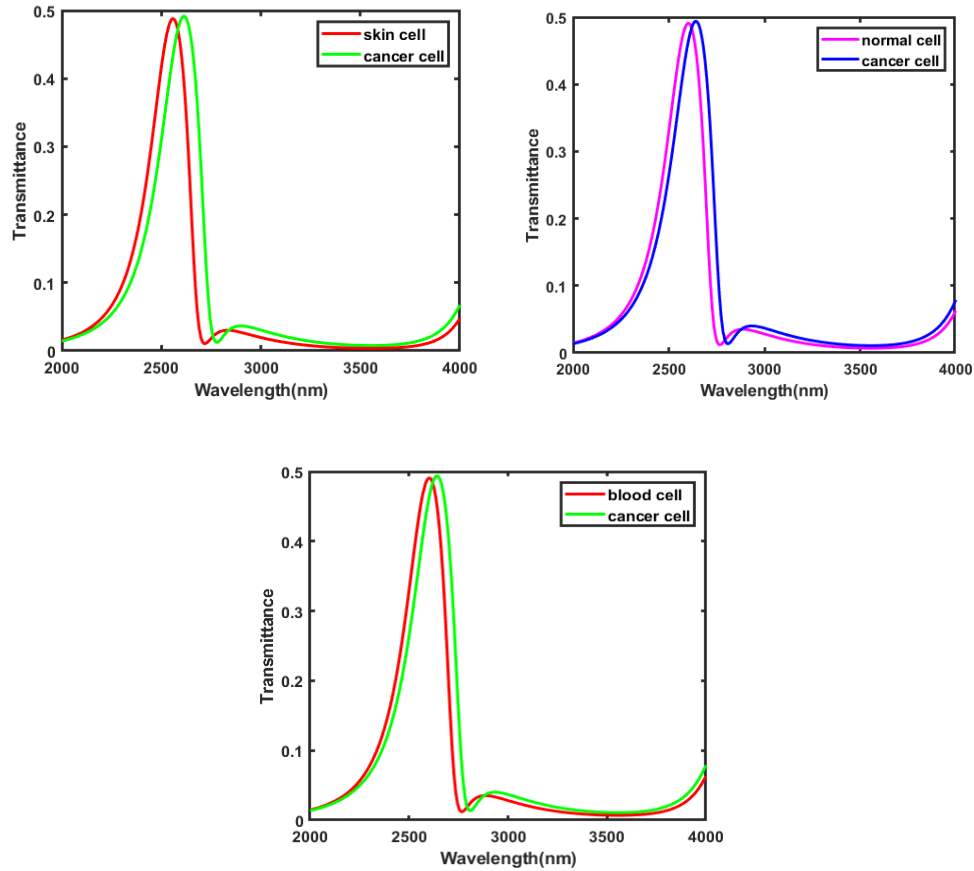


Figure 5.12 Performance of the optimized sensor for detecting (a)Skin Cancer, (b)Breast Cancer, (c)Blood Cancer

5.3.5 Conclusion

The structural parameters L_r , W_c , G , and D of the proposed sensor are tuned at values 440 nm, 29 nm, 25 nm and, 20 nm to leverage the maximum sensitivity of 4859 nm/RIU. The sensor presented makes use of the linear relationship between the refractive index and the resonant wavelength to identify unfamiliar materials. The possibility of the proposed RI sensor as a glucose sensor is also investigated by filling up the semi-circular cavity with differently concentrated glucose solution, and a linear shift in the transmission peak is observed. Therefore, the optimized design can be well considered as a potential candidate in the field of chemicals and biosensors.

5.4 Our Proposed Structure 2

5.4.1 Basic Structure

Taking inspiration from the first structure as illustrated in fig-, we modified our structure according to figure-. The resulting plasmonic sensor now features a two-dimensional schematic that includes input and output MIM waveguides. These waveguides are coupled with two concentric semicircle-shaped resonators. Additionally, we have incorporated a tunable baffle between the two waveguides. In the revised structure, the silver (Ag) is represented by the green shaded area, while the white shaded zone indicates the material under sensing (MUS).

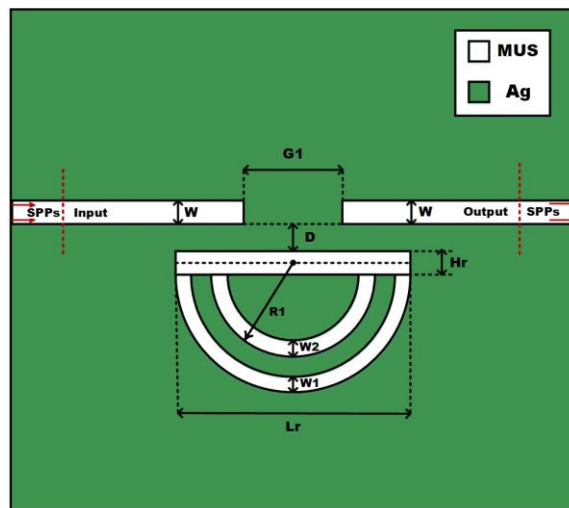


Figure 5.13 Two-dimensional (2D) schematic of the proposed RI sensor

The plasmonic sensor design incorporates various parameters with their respective symbols and values. The distance between the waveguide and resonator, denoted as D , is set at 20 nm. The diameter of the outer semicircle, represented by L_r , measures 400 nm. The width of the rectangular cavity, indicated as H_r , is specified as 25 nm. The outer semi-circular cavity has a width denoted as W_1 , measuring 25 nm, while the inner semi-circular cavity, with a width denoted as W_2 , measures 29 nm. The width of the waveguide, symbolized as W , is set at 20 nm. A baffle, denoted as G_1 , is incorporated and measures 50 nm. Lastly, the radius of the inner circle, represented by R_1 , is specified as 154 nm. These are listed in Table 5.5

These parameters collectively determine the dimensions and geometries of the plasmonic sensor structure, contributing to its functionality in capturing and manipulating plasmonic signals for various sensing applications.

Table 5.6 Initial structural Parameters of the sensor

Parameters	Symbols	Values (nm)
Distance between waveguide and resonator	D	20
The diameter of the outer semicircle	L_r	400
Width of the rectangular cavity	H_r	25
Width of the outer semi-circular cavity	W_1	25
Width of the inner semi-circular cavity	W_2	29
Width of the waveguide	W	20
Baffle	G_1	50
Radius of the inner circle	R_1	154

5.4.2 Initial Results

Initially, we conducted a simulation for the refractive index range of 1 to 1.05 with an interval of 0.01. This simulation was performed across the wavelength range of 2000 nm to 4000 nm, and the resulting transmittance peaks were observed. Figure 5.14 depicts the obtained transmittance peaks

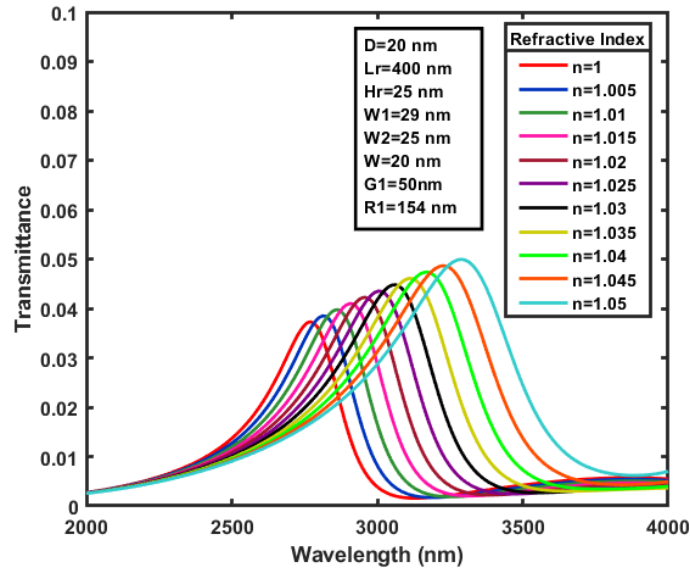


Figure 5.14 The transmittance peaks obtained for the initial parameters for 1 to 1.05 refractive index between wavelength 2000 nm to 4000 nm

Table 5.7 Sensitivity Analysis for n=1 to 1.05 between 2000 nm to 4000 nm

Refractive Indices	Resonant Peaks (nm)	Sensitivity(nm/RIU)
1	2773	
1.005	2813	7840
1.01	2863	10117
1.015	2905	8360
1.02	2959	10799
1.025	3004	8933
1.03	3061	11553
1.035	3122	12006

1.04	3171	9949
1.045	3223	10271
1.05	3289	13316

Remarkably, we achieved excellent sensitivity in our results, which is documented in the provided Table 5.7. We observed a highest sensitivity of 13316 nm/RIU for the change of refractive index from 1.045 to 1.05.

In this investigation, simulations were performed for refractive indices ranging from 1 to 1.05, covering a wavelength range of 800 to 2000 nm. The results revealed the presence of three additional modes compared to the initial case as shown in Figure 5.15. Notably, each mode exhibited a shift in transmittance peaks in response to changes in the wavelength.

However, it was observed from Table 5.8 that the sensitivity of these three modes was comparatively lower when compared to the first case. Despite this, the obtained sensitivities remained within acceptable ranges, providing valuable insights into the system. Specifically, the first mode displayed the highest sensitivity at 894 nm/RIU (refractive index unit), followed by the second mode at 1538 nm/RIU, and the third mode at 1777 nm/RIU.

These findings suggest that although the sensitivity of the three additional modes was slightly diminished compared to the initial case, their contributions were still noteworthy. Therefore, the analysis of these modes contributes to a more comprehensive understanding of the underlying dynamics and behavior of the system.

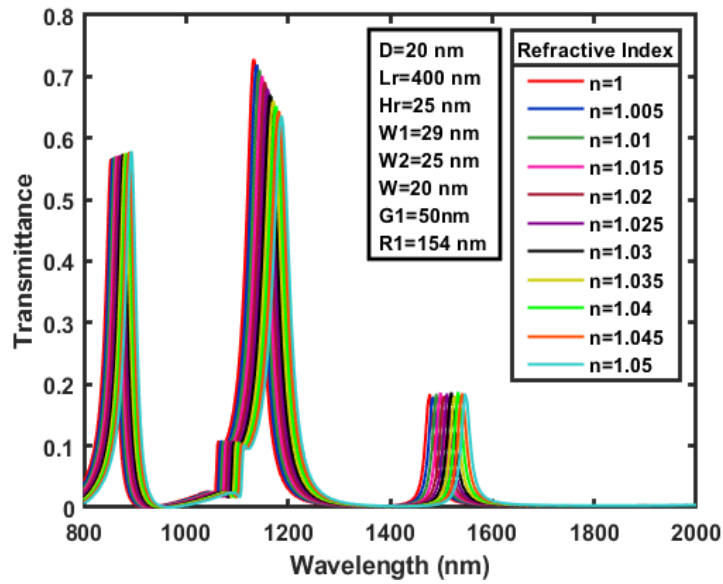


Figure 5.15 The transmittance peaks obtained for the initial parameters for 1 to 1.05 refractive index between wavelength 800 nm to 2000 nm

Table 5.8 Sensitivity Analysis for $n=1$ to 1.05 between 2000 nm to 4000 nm

n	Resonant Peaks			Sensitivity		
	Mode1	Mode2	Mode3	Mode1	Mode2	Mode3
1	853	1132	1478			
1.005	857	1139	1486	824	1454	1651
1.01	861	1144	1490	832	979	832
1.015	865	1149	1499	840	988	1679
1.02	869	1154	1507	848	997	1698
1.025	872	1159	1511	570	1006	856
1.03	876	1164	1520	862	1014	1727
1.035	881	1172	1529	871	1538	1747
1.04	885	1177	1533	879	1037	881

1.045	888	1182	1542	591	1046	1777
1.05	893	1188	1547	894	1056	897

Subsequently, our investigation extended to exploring a range of refractive index values, specifically from 1.2 to 1.3, 1.3 to 1.4, and 1.4 to 1.5. We sought to identify different modes within these index ranges, with the aim of achieving improved sensitivity.

For the range of 1.2 to 1.3, we identified two distinct modes spanning the wavelength range of 1200 nm to 2200 nm, as depicted in Figure 5.16. Both modes exhibited notable changes in transmittance peaks in response to variations in wavelength. The refractive index was systematically incremented from 1.2 to 1.3 at an interval of 0.01. Notably, the highest sensitivity observed for this range was 1684 nm/RIU for mode 2 as found out from the Table 5.9. These findings suggest that by exploring refractive index ranges and corresponding wavelength values, we were able to identify multiple modes exhibiting satisfactory sensitivity.

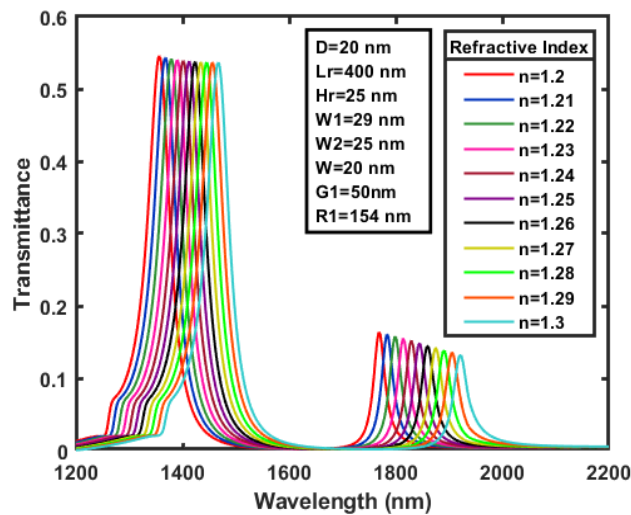


Figure 5.16 The transmittance peaks obtained for the initial parameters for 1.2 to 1.3 refractive index between wavelength 1200 nm to 2200 nm

Table 5.9 Sensitivity Analysis for n=1.2 to 1.3 between 1200 nm to 2200 nm

n	Resonant Peaks		Sensitivity	
	Mode1	Mode2	Mode1	Mode2
1	1356	1767		
1.005	1368	1782	1233	1496
1.01	1379	1798	1075	1521
1.015	1390	1813	1092	1548
1.02	1401	1829	1109	1575
1.025	1413	1845	1127	1602
1.03	1424	1858	1145	1302
1.035	1433	1874	968	1654
1.04	1445	1891	1180	1684
1.045	1457	1905	1199	1369
1.05	1467	1919	1015	1389

In the subsequent phases of our study, we extended our simulations to encompass the refractive index ranges of 1.3 to 1.4 and 1.4 to 1.5. For the range of 1.3 to 1.4, the simulations were conducted over a wavelength range of 1400 nm to 2500 nm. Similarly, for the range of 1.4 to 1.5, the simulations spanned from 1400 nm to 3000 nm. It is important to note that the simulations were performed at multiple wavelengths; however, we have presented the specific wavelengths where better results and transmission peaks were observed for each refractive index range. The chosen interval between refractive indices remained consistent at 0.01. The obtained transmission profiles for both ranges are depicted in Figure 5.17 and Figure 5.18 respectively, providing a visual representation of the transmittance behavior at various wavelengths within the specified ranges.

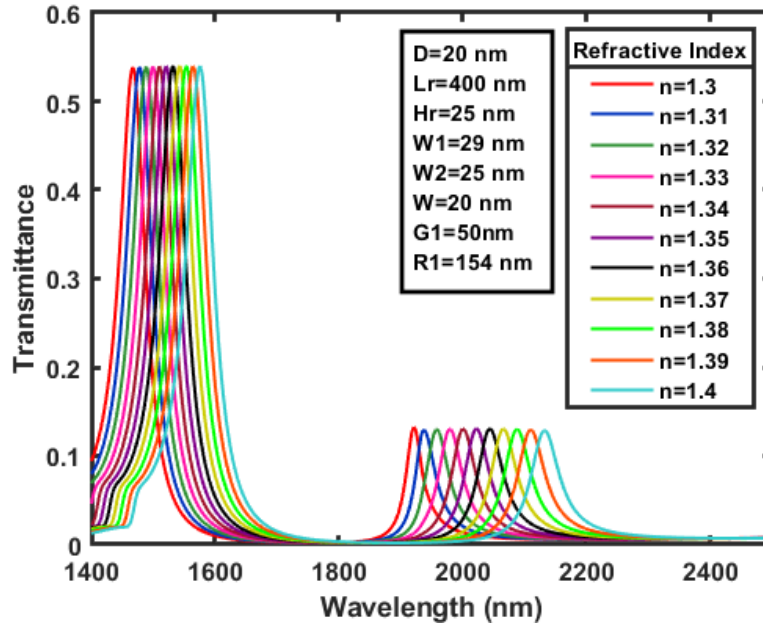


Figure 5.17 The transmittance peaks obtained for the initial parameters for 1.3 to 1.4 refractive index between wavelength 1400 nm to 2400 nm

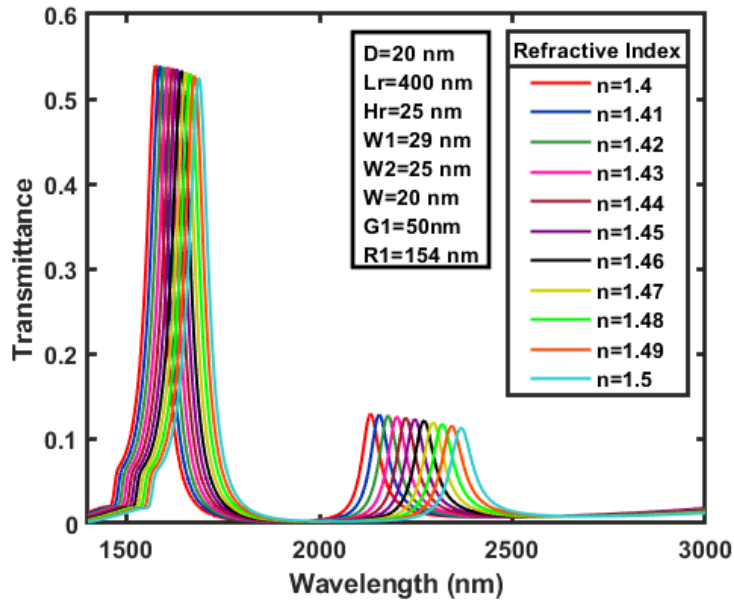


Figure 5.18 The transmittance peaks obtained for the initial parameters for 1.4 to 1.5 refractive index between wavelength 1400 nm to 3000 nm

5.4.3 Optimization of Initial Parameters

By keeping the refractive index (RI) value fixed at $n=1.03$, we decided to optimize the sensitivity of our system by altering the diameter of the outer semicircle, L_r . We varied the diameter from 400 to 430 nm in increments of 10 nm as shown in Figure 5.19. Interestingly, as we increased the diameter length, we observed a blue shift of the transmittance peaks. This indicates that the transmittance peaks shifted towards smaller wavelengths.

To further investigate the effect of diameter on sensitivity, we conducted simulations for each diameter, considering changes in the refractive index from 1 to 1.05 with an interval of 0.01 as illustrated in Figure 5.20. After analyzing the results, we computed the sensitivity for each case. We observed that the sensitivity decreased as the diameter increased. In fact, our initial diameter value of 400 nm provided the maximum sensitivity in this scenario. From Figure 5.21, it is evident that the sensitivity progressively decreased as we increased the diameter, reaffirming that our initial diameter choice of 400 nm was optimal for achieving the highest sensitivity in our system.

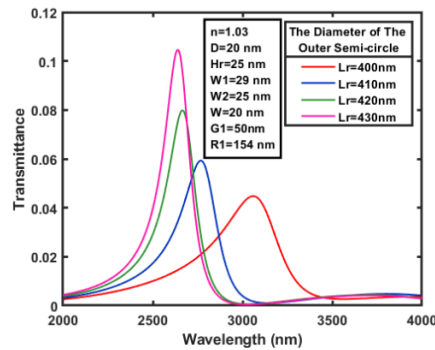
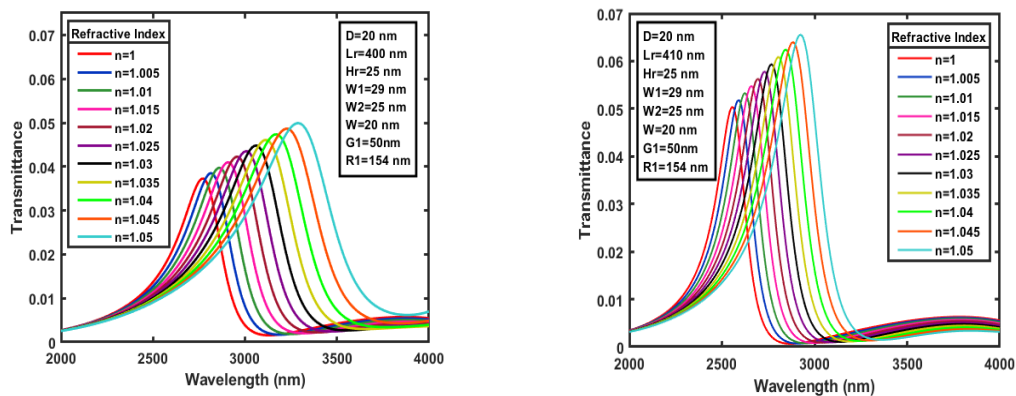


Figure 5.19 Transmittance spectrum for different diameter of outer semicircle, L_r



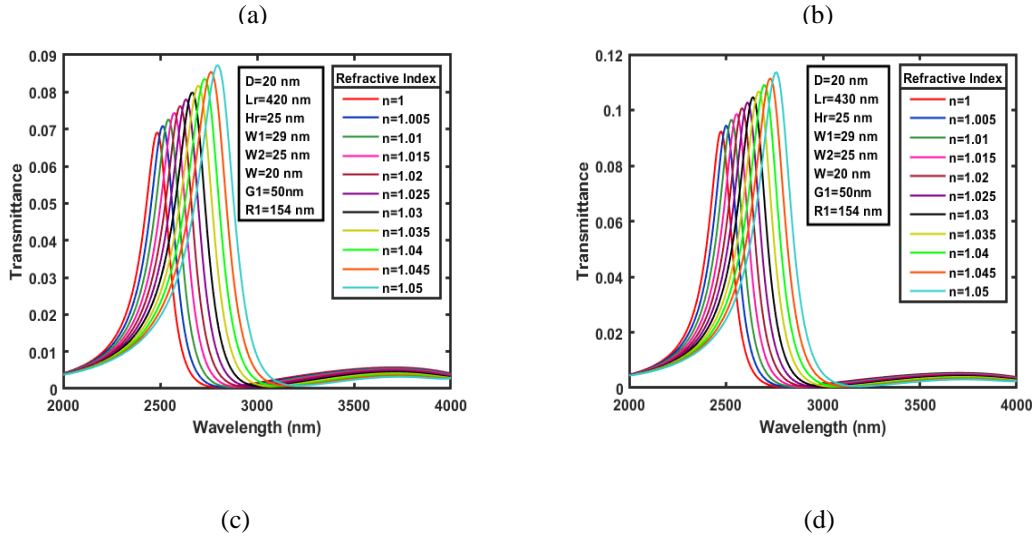


Figure 5.20 Transmission spectrum for different values of n between 1 to 1.05 at Lr (a) 400 nm, (b) 410 nm (c) 420 nm (d) 430 nm_

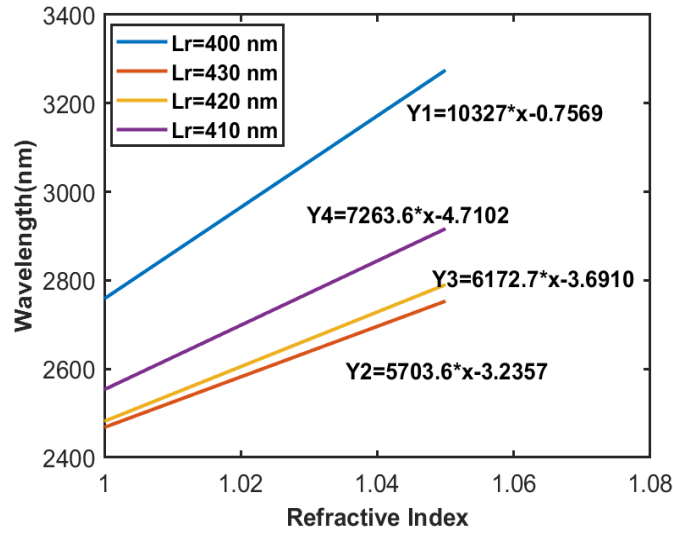


Figure 5.21 Sensitivity Comparison for different Values of Lr

In our pursuit of achieving better results, we decided to explore the possibility of decreasing the diameter value. This time, we varied the Lr values from 396 nm to 404 nm with an interval of 2 nm depicted in Figure 5.22. Surprisingly, as we decreased the diameter, we observed an increase in sensitivity. However, there was a trade-off: the transmittance peaks became progressively flatter, which reduced the overall sensing capability.

To strike a balance between sensitivity and performance, we carefully evaluated the transmittance peaks for intermediate values of 398 nm and 399 nm, considering the corresponding changes in

refractive indices as depicted in Figure 5.23. We aimed to identify a diameter value that provided a desirable combination of sensitivity and distinct transmittance peaks.

After thorough analysis as illustrated in Figure 5.24, taking both sensitivity and performance into account, we selected an optimal value of 399 nm as our updated parameter. This diameter value offered a notable increase in sensitivity while still maintaining reasonably distinguishable transmittance peaks.

Thus, our decision was driven by a careful consideration of both factors, ensuring an improved performance in our system.

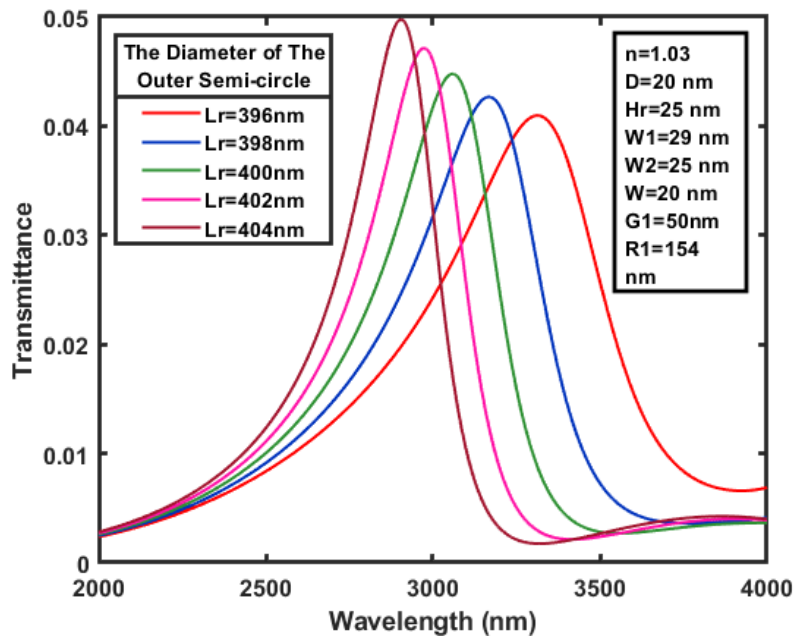
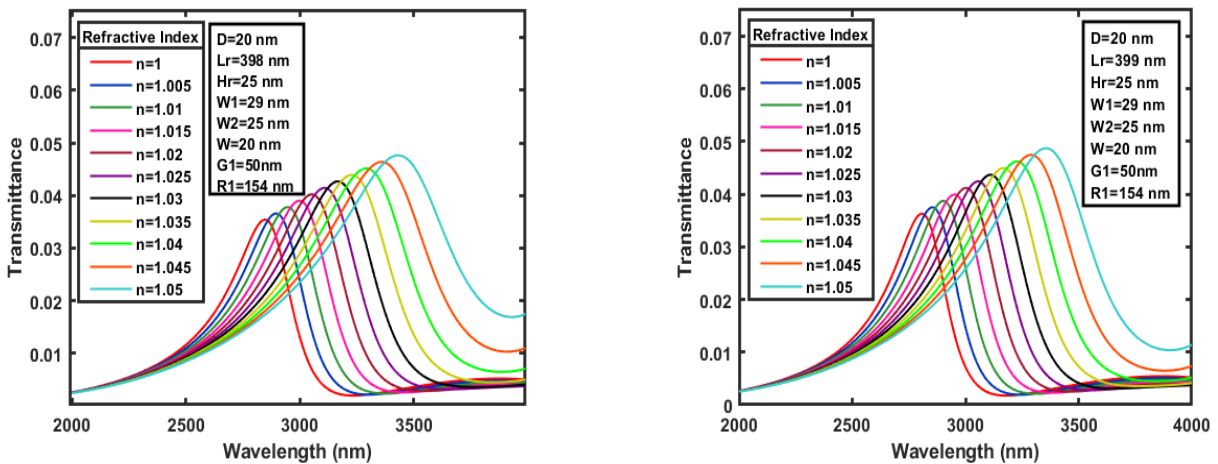


Figure 5.22 Transmittance spectrum for different diameter of outer semicircle, Lr



(a) (b)

Figure 5.23 Transmission spectrum for different values of n between 1 to 1.05 at Lr (a) 398 nm, (b) 399 nm

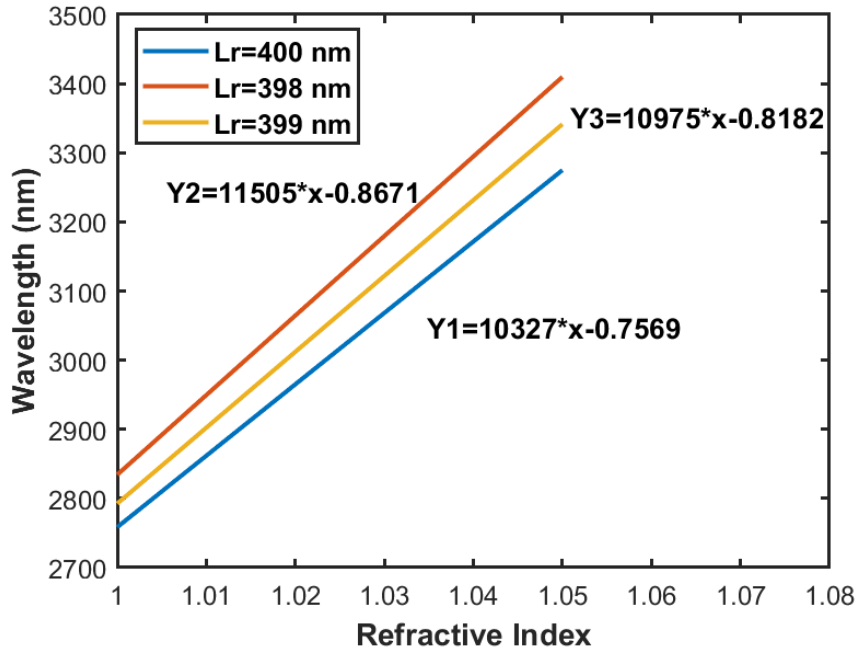


Figure 5.24 Sensitivity comparison for different values of Lr

In our quest for better results, we made a significant change by adjusting the distance between the waveguide and resonator, D. We decreased the distance from 20 nm to 10 nm, aiming to optimize the system's performance. This alteration had a noticeable impact on the overall behavior and sensitivity of the system. To further explore the tunability of our system, we focused on varying the width of the waveguide, W, in the range of 20 nm to 50 nm with an interval of 10 nm as shown in Figure 5.25. As we increased the width, we observed a progressive decrease in the transmittance values, accompanied by slight shifts of the corresponding peaks towards smaller wavelengths. This investigation allowed us to understand the influence of W on the overall behavior of the system and its potential for sensing applications.

To evaluate the performance of different waveguide widths for sensing changes in refractive indices, we conducted experiments for each value of W (20 nm, 30 nm, 40 nm, and 50 nm)

as shown in Figure 5.26.

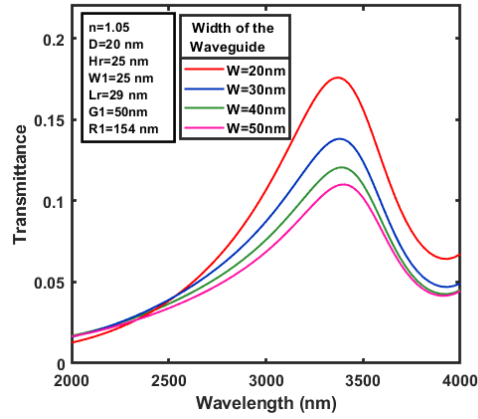


Figure 5.25 Transmittance spectrum for different width of the waveguide, W

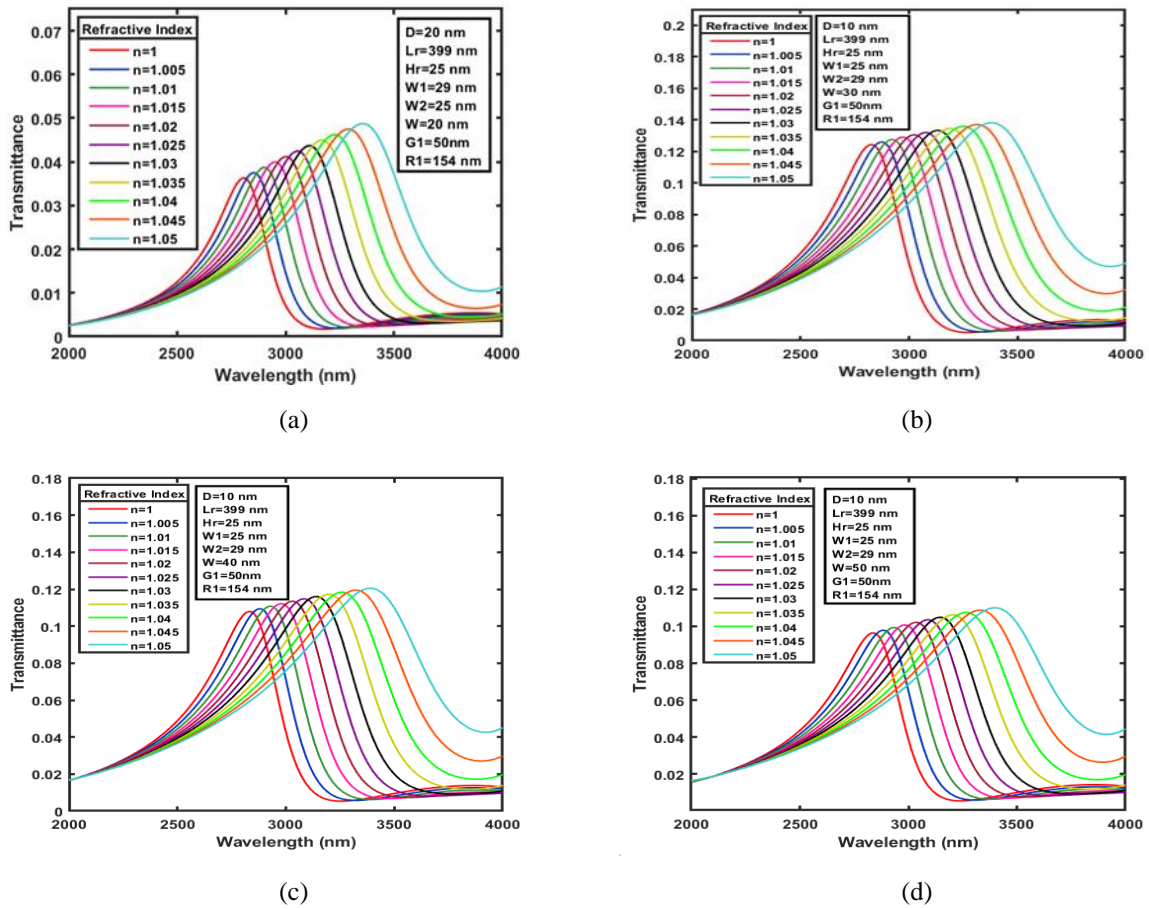


Figure 5.26 Transmission spectrum for different values of n between 1 to 1.05 at W (a) 20 nm, (b) 30 nm (c) 40 nm (d) 50 nm

For each case, we calculated the sensitivity and plotted it against the change in refractive indices. From the resulting graph in Figure 5.27, it became evident that the best results were obtained for the initial parameter of $W = 20$ nm. This particular width provided the highest sensitivity and demonstrated superior performance in our system.

Based on these comprehensive analyses, we made the decision to stick with our initial parameter of $W = 20$ nm, as it yielded the most favorable outcomes in terms of sensitivity and overall performance.

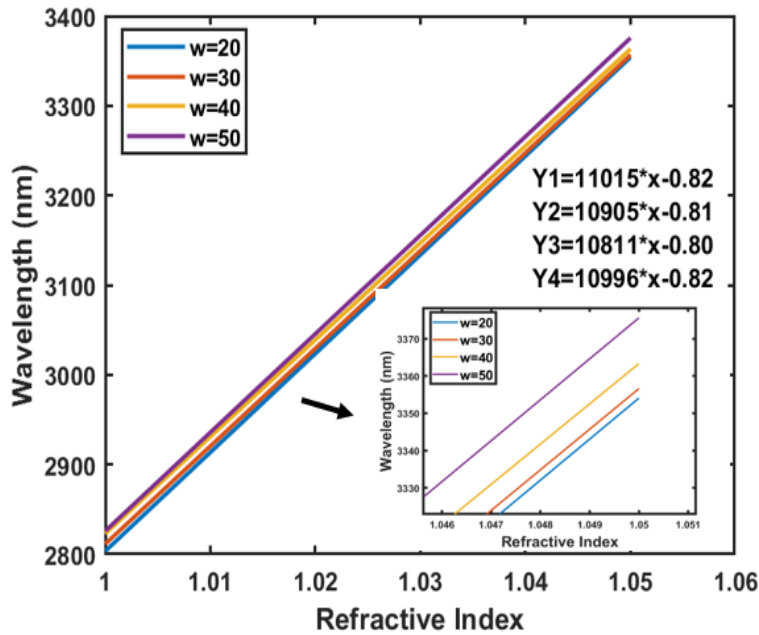


Figure 5.27 Sensitivity comparison for different values of W

Following the previous adjustments, we altered the radius of the inner circle, $R1$, to optimize the system's performance. We conducted a parametric sweep in COMSOL Multiphysics, ranging from 150 nm to 154 nm with an increment of 1 nm, as shown in Figure 5.28. Intriguingly, as we decreased the radius, we observed a consistent shift of the transmittance peaks towards smaller wavelengths.

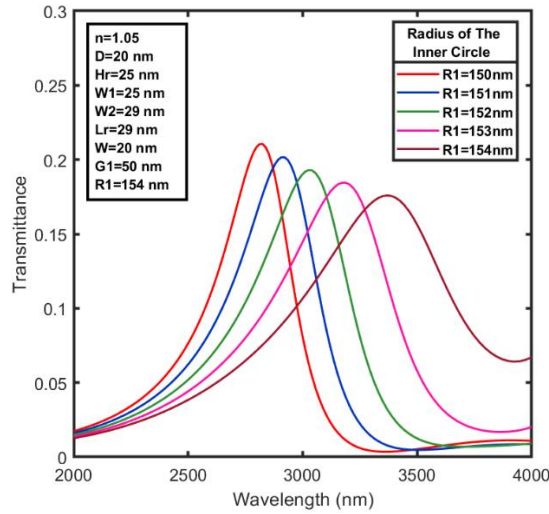


Figure 5.28 Transmittance spectrum for different radius of the inner circle, R1

Additionally, we investigated the influence of these changes in the sensor's dimensions on the system's ability to sense changes in refractive indices. Figure 5.29 and Figure 5.30 provides a visual representation of the transmittance peaks for each of the R1 values, including 150 nm, 151 nm, 152 nm, 153 nm, and 154 nm.

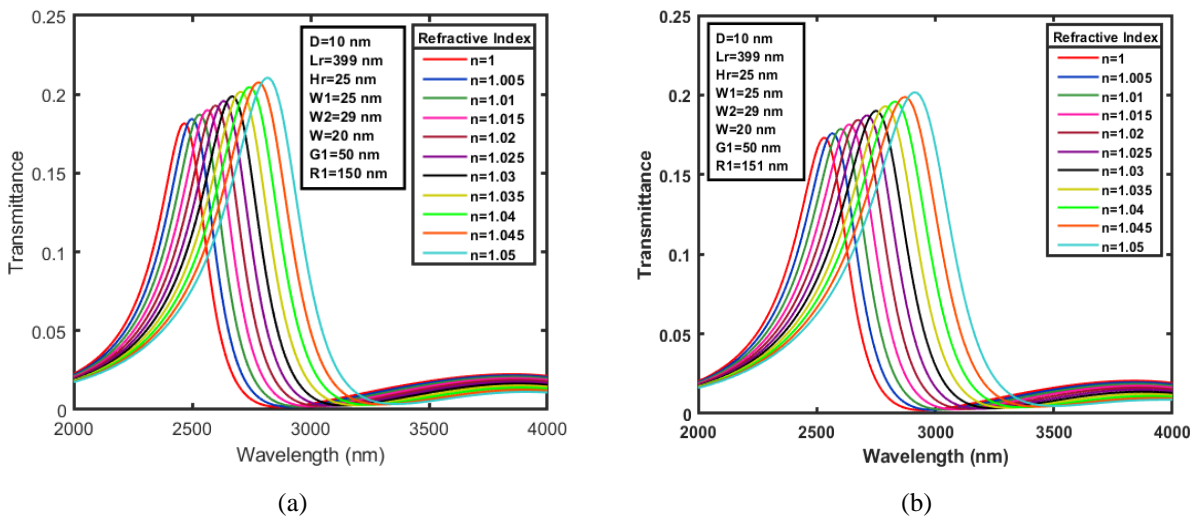


Figure 5.29 Transmission spectrum for different values of n between 1 to 1.05 at R1
(a) 150 nm, (b) 151 nm

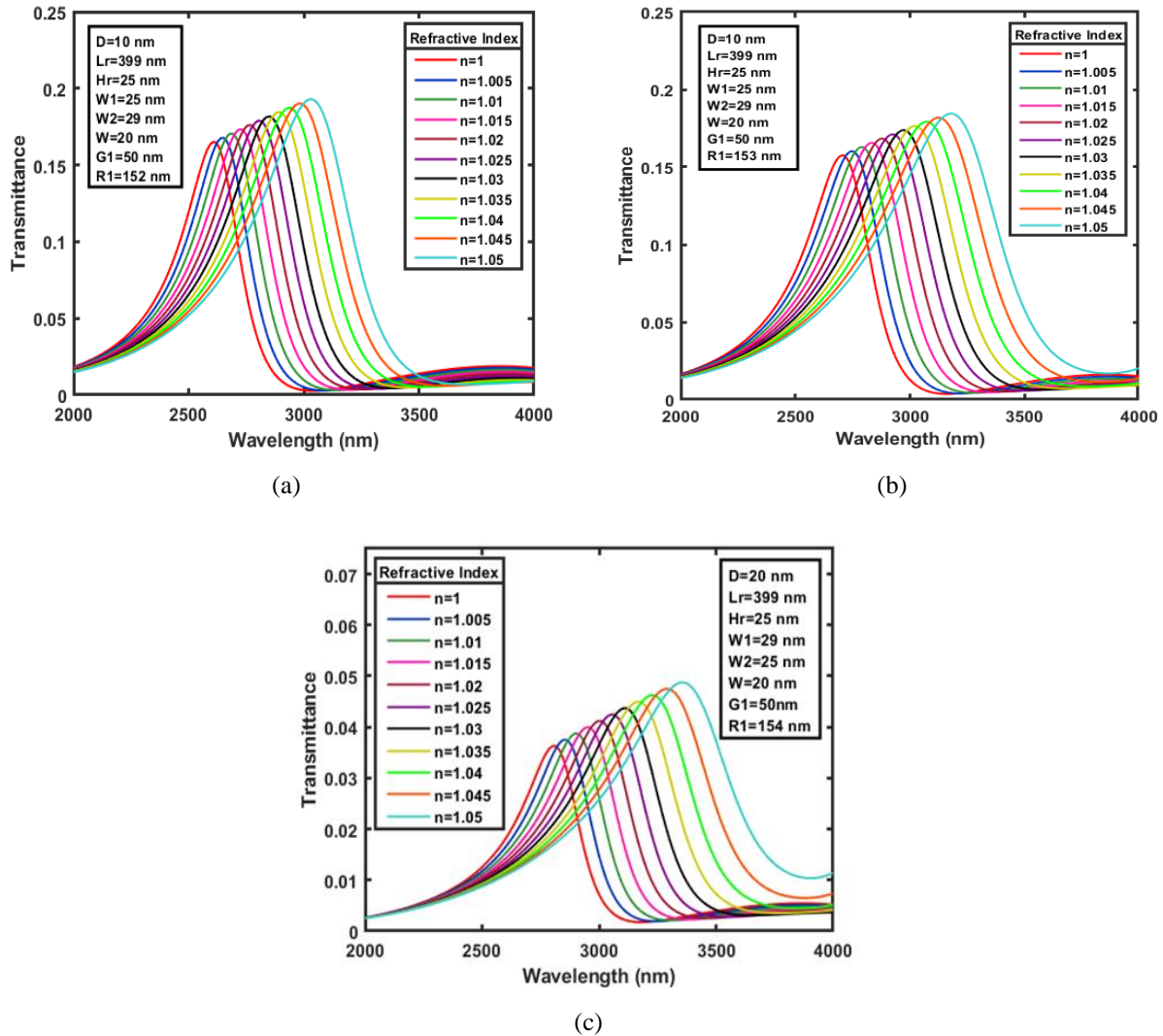


Figure 5.30 Transmission spectrum for different values of n between 1 to 1.05 at R_1 (a) 152 nm, (b) 153 nm (c) 154 nm

Through a careful examination of these results as shown in Figure 5.31, we reached the conclusion that altering the R_1 value from its initial setting had a detrimental effect on either the sensitivity or the sharpness of the peaks.

Considering both the sensitivity and the distinctness of the transmittance peaks, we determined that a fixed R_1 value of 154 nm provided the optimized performance for our system. This decision was made based on a thorough analysis of the obtained results, ensuring that the chosen parameter value maintained the desired sensitivity and peak sharpness.

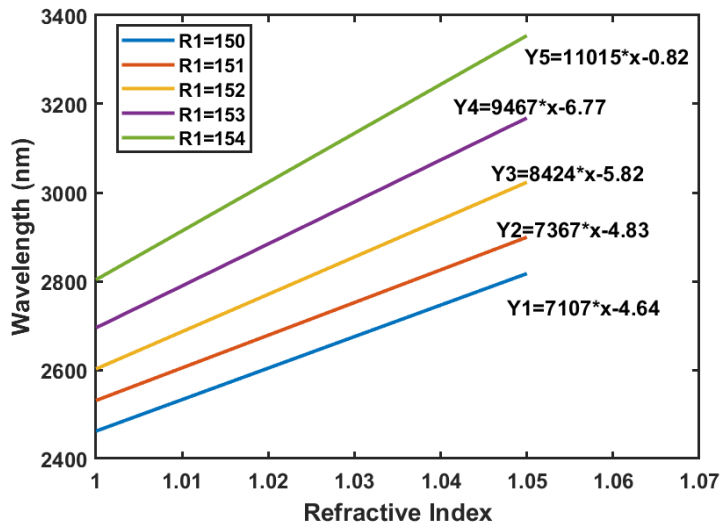


Figure 5.31 Sensitivity comparison for different values of R1

In order to enhance the performance of our system, we decided to make adjustments to the width of the outer semi-circular cavity, W1. By systematically varying W1 from 23 nm to 26 nm with a 1 nm increment, we aimed to observe its effect on the system's behavior. Notably, as we increased the width, we observed a distinctive phenomenon known as a red shift in the transmittance peaks in Figure 5.32. This shift indicated a noticeable displacement of the peaks towards longer wavelengths, suggesting changes in the system's spectral response.

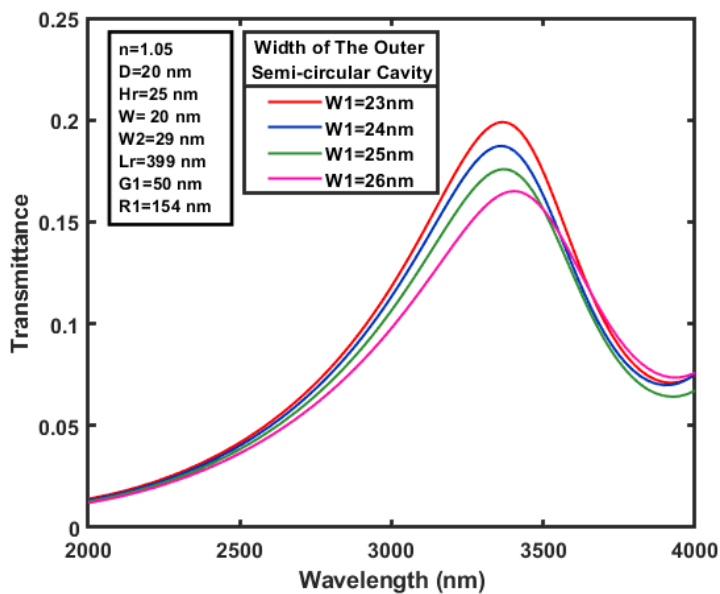


Figure 5.32 Transmittance spectrum for different width of the outer semi-circular cavity, W1

To further evaluate the impact of these parameter changes on the system's sensitivity to changes in refractive indices, we plotted its transmittance characteristics for each if the W1 values as shown in Figure 5.33.

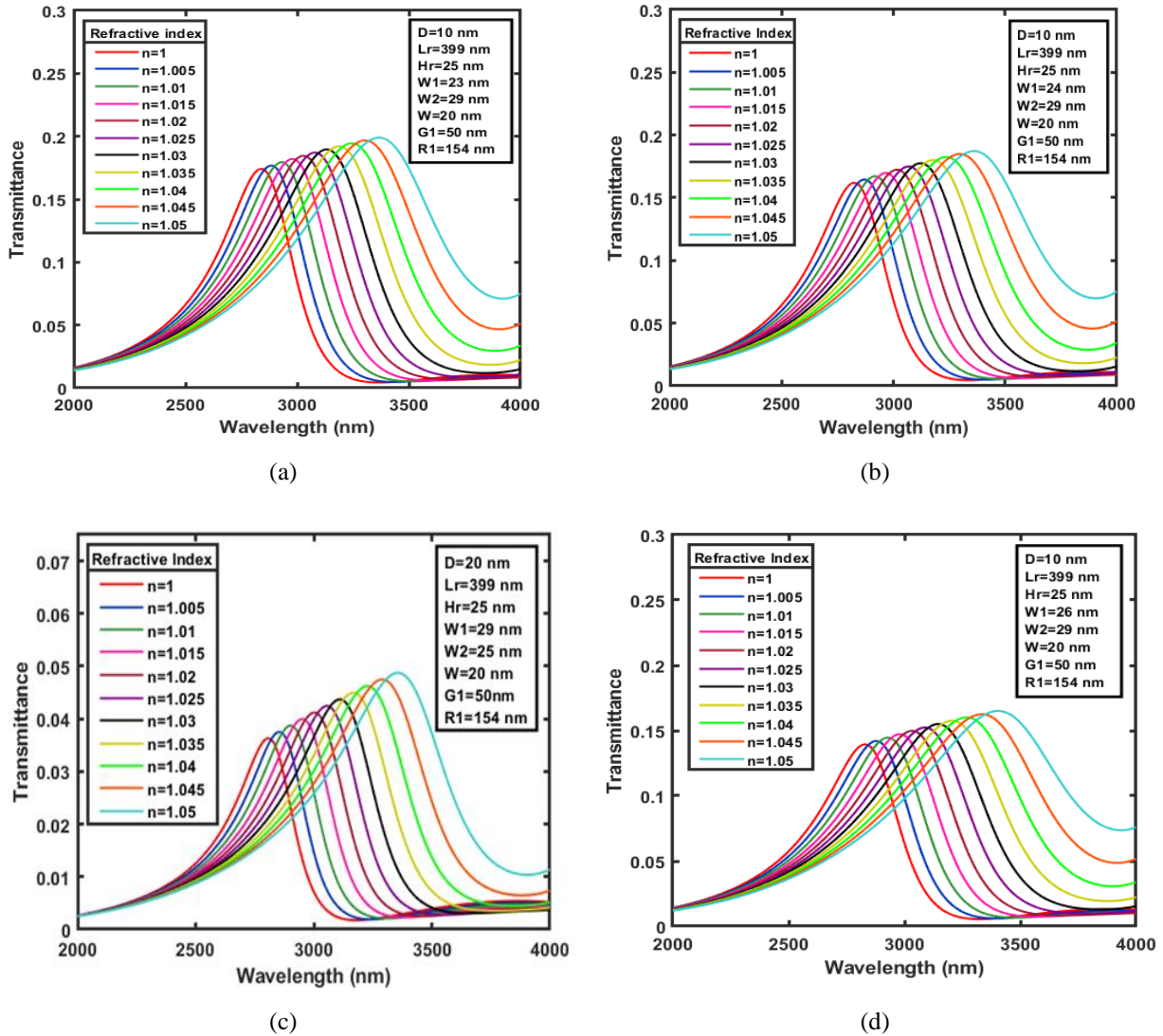


Figure 5.33 Transmission spectrum for different values of n between 1 to 1.05 at $W1$ (a) 23 nm, (b) 24 nm (c) 25 nm (d) 26 nm

A graph of wavelength versus refractive index, as shown in Figure X. This graph provided insights into the relationship between the varying $W1$ values and the resulting sensitivity of the system.

Upon careful analysis of the graph in Figure 5.34, we observed that for $W1 = 26$ nm, we obtained the largest slope, indicating the highest sensitivity. Therefore, based on these findings, we concluded that $W1 = 26$ nm is the optimized value for our system. This particular width configuration demonstrated superior performance in terms of sensitivity, reaffirming its selection as the optimal parameter.

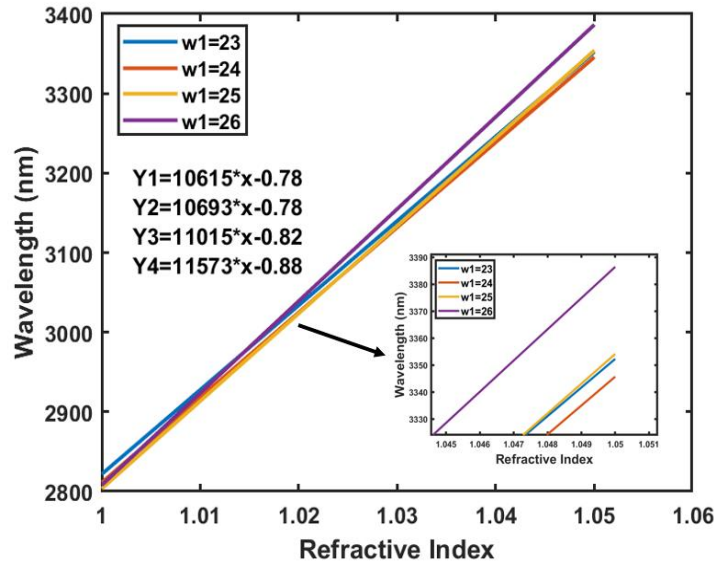


Figure 5.34 Sensitivity comparison for different values of $W1$

In our final set of modifications, we focused on adjusting the width of the inner semi-circular cavity, $W2$. By systematically varying $W2$ from 27 nm to 30 nm with a 1 nm interval, we sought to understand its impact on the system's performance.

From our observations in Figure 5.35, it became apparent that decreasing the width of the inner semi-circular cavity resulted in a severe degradation of performance. Therefore, we decided to conduct further investigations only for the values of $W2$ at 29 nm and 30 nm, as these exhibited more promising results. The transmission spectrum for values 29 nm and 30 nm are illustrated in Figure 5.36.

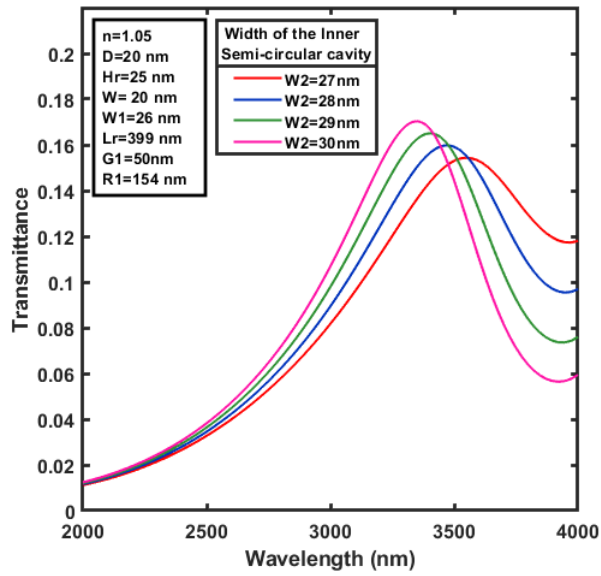


Figure 5.35 Transmittance spectrum for different width of the inner semi-circular cavity, W_2

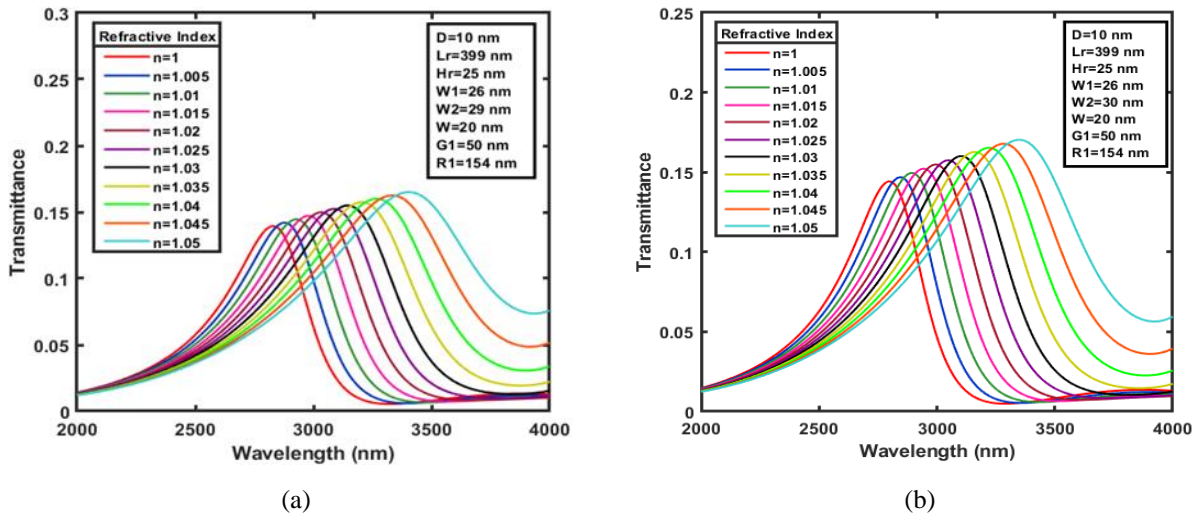


Figure 5.36 Transmission spectrum for different values of n between 1 to 1.05 at W_2 (a) 29 nm, (b) 30 nm

After careful analysis of the data presented in Figure 5.37, we arrived at the conclusion that our initial value of 29 nm for the width of the inner semi-circular cavity is the most optimal choice.

This determination was made considering the overall performance of the system, as it offered the best compromise between sensitivity and other desired characteristics. Thus, we selected 29 nm as the most suitable width for the inner semi-circular cavity in our optimized configuration.

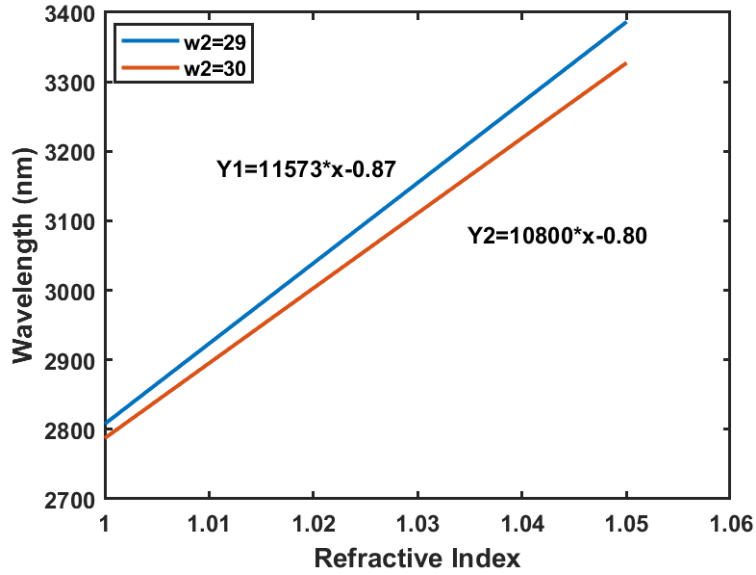


Figure 5.37 Sensitivity comparison for different values of W2

Table 5.10 Optimized structural Parameters of the sensor

Parameters	Symbols	Values (nm)
Distance between waveguide and resonator	D	10
The diameter of the outer semicircle	Lr	399
Width of the rectangular cavity	Hr	25
Width of the outer semi-circular cavity	W1	26
Width of the inner semi-circular cavity	W2	29
Width of the waveguide	W	20
Baffle	G1	50
Radius of the inner circle	R1	154

5.4.4 Conclusion

The proposed sensor has been carefully designed with specific structural parameters. The diameter of the outer semicircle (L_r) is set at 399 nm, distance between waveguide and resonator (D) at 10 nm, the waveguide width (W) at 20 nm, the radius of the inner circle (R_1) at 154 nm, and the widths of the outer and inner semicircular cavity sections (W_1 and W_2) at 26 nm and 29 nm, respectively.

By tuning these parameters, the sensor achieves maximum sensitivity of 11573 nm/RIU within the refractive index range of 1 to 1.05, which is particularly suitable for gas sensing applications. Furthermore, the sensor exhibits satisfactory performance across other refractive index ranges, including 1.2 to 1.3, 1.3 to 1.4, and 1.4 to 1.5, which correspond to various biosensing regions.

The sensor capitalizes on the linear relationship between the refractive index of the medium and the resonant wavelength to identify unfamiliar materials. By filling the concentric semi-circular cavity with different unknown solutions, a linear shift in the transmission peak is observed. This shift in the resonant wavelength provides valuable information about the refractive index of the unknown solutions, enabling their identification and characterization.

Considering its optimized design and demonstrated performance, this sensor holds significant potential in the fields of gas sensing and biosensing. Its ability to accurately detect and analyze unknown substances makes it a promising candidate for a wide range of applications in chemical and biological sensing.

Chapter 6

Conclusion and Future Works

6.1 Conclusion:

This thesis work illustrates a nanosensor based on SPPs in MIM waveguides with two structures with the aim of enhancing the sensitivity of the sensors.

The initial structure is composed of a semi-circular ring with a baffle between the pair of the waveguide. COMSOL Multiphysics, which inherently employs the FEM for numerical analysis, was used to model the described nanosensor. After extensive reruns of simulations, the optimized parameters L_r , W_c , G , and D have tuned at values 440 nm, 29 nm, 25 nm, and, 20 nm to leverage the maximum sensitivity of 4859 nm/RIU.

The sensor presented makes use of the linear relationship between the refractive index and the resonant wavelength to identify unfamiliar materials. The possibility of the proposed RI sensor as a glucose sensor is also investigated by filling up the semi-circular cavity with differently concentrated glucose solution, and a linear shift in the transmission peak is observed. Therefore, the optimized design can be well considered as a potential candidate in the field of chemicals and biosensors.

After modifying our initial structure, the proposed sensor has been modeled with specific structural parameters L_r , D , W , R_1 , W_1 , and W_2 have tuned to 399 nm, 10 nm, 20 nm, 154 nm, 26 nm, and 29 nm, respectively.

After tuning these parameters maximum sensitivity of the sensor becomes 11573 nm/RIU within the refractive index range of 1 to 1.05. This range is used for gas-sensing applications. Again, in other ranges, the sensor also shows high sensitivity which has also applications in cancer cell detection, virus detection, biomarker detection etc.

6.2 Future Works:

The following steps can be taken as the future works for this thesis:

- For this work silver is used, other metals can be taken into consideration to check the performance of the RI sensors.
- Incorporation of nanodots and nanorods in the sensor structure can be analyzed.
- Determination of some other performance parameters of sensors. For example, quality factor, FOM, resolution etc of the nano-sensor.

References

- [1] R. Al Mahmud, M. O. Faruque, and R. H. Sagor, “Plasmonic Refractive Index Sensor Based on Ring-Type Pentagonal Resonator with High Sensitivity,” *Plasmonics*, vol. 16, no. 3, pp. 873–880, 2021, doi: 10.1007/s11468-020-01357-7.
- [2] F. Vollmer and D. Yu, “Surface Plasmon Resonance,” 2020, pp. 61–115. doi: 10.1007/978-3-030-60235-2_2.
- [3] R. Al Mahmud, M. O. Faruque, and R. H. Sagor, “A highly sensitive plasmonic refractive index sensor based on triangular resonator,” *Opt Commun*, vol. 483, Mar. 2021, doi: 10.1016/j.optcom.2020.126634.
- [4] Y. Zhang *et al.*, “High-sensitivity refractive index sensors based on Fano resonance in the plasmonic system of splitting ring cavity-coupled MIM waveguide with tooth cavity,” *Appl Phys A Mater Sci Process*, vol. 125, no. 1, p. 0, 2019, doi: 10.1007/S00339-018-2283-0.
- [5] M. F. Hassan, I. Tathfif, M. Radoan, and R. H. Sagor, “A concentric double-ring resonator based plasmonic refractive index sensor with glucose sensing capability,” in *IEEE Region 10 Annual International Conference, Proceedings/TENCON*, Institute of Electrical and Electronics Engineers Inc., Nov. 2020, pp. 91–96. doi: 10.1109/TENCON50793.2020.9293901.
- [6] M. R. Rakhshani and M. A. Mansouri-Birjandi, “Dual wavelength demultiplexer based on metal-insulator-metal plasmonic circular ring resonators,” *J Mod Opt*, vol. 63, no. 11, pp. 1078–1086, Jun. 2016, doi: 10.1080/09500340.2015.1125962.
- [7] Z. Zhang *et al.*, “Plasmonic refractive index sensor with high figure of merit based on concentric-rings resonator,” *Sensors (Switzerland)*, vol. 18, no. 1, Jan. 2018, doi: 10.3390/s18010116.
- [8] S. C. Kilic and S. Kocaman, “High Sensitivity Fano-Like Rod-Type Silicon Photonic Crystal Refractive Index Sensor,” in *2020 14th International Congress on Artificial Materials for Novel Wave Phenomena, Metamaterials 2020*, Institute of Electrical and Electronics Engineers Inc., Sep. 2020, pp. 385–387. doi: 10.1109/Metamaterials49557.2020.9285020.
- [9] S. Zou, F. Wang, R. Liang, L. Xiao, and M. Hu, “A nanoscale refractive index sensor based on asymmetric plasmonic waveguide with a ring resonator: A review,” *IEEE Sens J*, vol. 15, no. 2, pp. 646–650, Feb. 2015, doi: 10.1109/JSEN.2014.2364251.
- [10] J. H. Zhu, Q. J. Wang, P. Shum, and X. G. Huang, “A nanoplasmonic high-pass wavelength filter based on a metal-insulator- metal circuitous waveguide,” *IEEE Trans Nanotechnol*, vol. 10, no. 6, pp. 1357–1361, Nov. 2011, doi: 10.1109/TNANO.2011.2136385.

- [11] Stefan A. Maier, *PLASMONICS_Fundamentals and Applications_Maier_Springer 2006*. 2007.
- [12] M. A. Jabin *et al.*, “Surface Plasmon Resonance Based Titanium Coated Biosensor for Cancer Cell Detection,” *IEEE Photonics J*, vol. 11, no. 4, p. 1, 2019, doi: 10.1109/JPHOT.2019.2924825.
- [13] S. Rohimah *et al.*, “Fano Resonance in the Plasmonic Structure of MIM Waveguide with r-Shaped Resonator for Refractive Index Sensor,” *Plasmonics*, vol. 17, no. 4, pp. 1681–1689, 2022, doi: 10.1007/s11468-022-01655-2.
- [14] A. Harhouz and A. Hocini, “Highly sensitive plasmonic temperature sensor based on Fano resonances in MIM waveguide coupled with defective oval resonator,” *Opt Quantum Electron*, vol. 53, no. 8, 2021, doi: 10.1007/s11082-021-03088-3.
- [15] K. S. Rashid, M. F. Hassan, A. A. Yaseer, I. Tathfif, and R. H. Sagor, “Gas-sensing and label-free detection of biomaterials employing multiple rings structured plasmonic nanosensor,” *Sens Biosensing Res*, vol. 33, p. 100440, 2021, doi: 10.1016/j.sbsr.2021.100440.
- [16] Y. Zhang and M. Cui, “Refractive Index Sensor Based on the Symmetric MIM Waveguide Structure,” *J Electron Mater*, vol. 48, no. 2, pp. 1005–1010, 2019, doi: 10.1007/s11664-018-6823-3.
- [17] X. Yang, E. Hua, M. Wang, Y. Wang, F. Wen, and S. Yan, “Fano resonance in a mim waveguide with two triangle stubs coupled with a split-ring nanocavity for sensing application,” *Sensors (Switzerland)*, vol. 19, no. 22, Nov. 2019, doi: 10.3390/s19224972.
- [18] X. Zhang, Y. Qi, P. Zhou, H. Gong, B. Hu, and C. Yan, “Refractive Index Sensor Based on Fano Resonances in Plasmonic Waveguide With Dual Side-Coupled Ring Resonators,” *Photonic Sensors*, vol. 8, no. 4, pp. 367–374, 2018, doi: 10.1007/s13320-018-0509-6.
- [19] X. Zhang, M. Shao, and X. Zeng, “High quality plasmonic sensors based on fano resonances created through cascading double asymmetric cavities,” *Sensors (Switzerland)*, vol. 16, no. 10, 2016, doi: 10.3390/s16101730.
- [20] N. Jankovic and N. Cselyuszka, “Multiple fano-like MIM plasmonic structure based on triangular resonator for refractive index sensing,” *Sensors (Switzerland)*, vol. 18, no. 1, Jan. 2018, doi: 10.3390/s18010287.
- [21] M. F. Hassan, R. H. Sagor, M. R. Amin, M. R. Islam, and M. S. Alam, “Point of Care Detection of Blood Electrolytes and Glucose Utilizing Nano-Dot Enhanced Plasmonic Biosensor,” *IEEE Sens J*, vol. 21, no. 16, pp. 17749–17757, 2021, doi: 10.1109/JSEN.2021.3082756.
- [22] K. S. Rashid, I. Tathfif, A. A. Yaseer, Md. F. Hassan, and R. H. Sagor, “Cog-shaped refractive index sensor embedded with gold nanorods for temperature sensing of multiple analytes,” *Opt Express*, vol. 29, no. 23, p. 37541, 2021, doi: 10.1364/oe.442954.

- [23] R. Zafar and M. Salim, “Enhanced Figure of Merit in Fano Resonance-Based Plasmonic Refractive Index Sensor,” *IEEE Sens J*, vol. 15, no. 11, pp. 6313–6317, 2015, doi: 10.1109/JSEN.2015.2455534.
- [24] Y. Zhang *et al.*, “High-sensitivity refractive index sensors based on Fano resonance in the plasmonic system of splitting ring cavity-coupled MIM waveguide with tooth cavity,” *Applied Physics A*, vol. 125, no. 1, Jan. 2019, doi: 10.1007/s00339-018-2283-0.
- [25] X. Yi, J. Tian, and R. Yang, “Tunable Fano resonance in plasmonic MDM waveguide with a square type split-ring resonator,” *Optik (Stuttg)*, vol. 171, pp. 139–148, 2018, doi: 10.1016/j.ijleo.2018.06.027.
- [26] Z. Zhang, L. Luo, C. Xue, W. Zhang, and S. Yan, “Fano resonance based on metal-insulator-metal waveguide-coupled double rectangular cavities for plasmonic nanosensors,” *Sensors (Switzerland)*, vol. 16, no. 5, pp. 22–24, 2016, doi: 10.3390/s16050642.
- [27] J. Zhou *et al.*, “Transmission and refractive index sensing based on fanoresonance in MIM waveguide-coupled trapezoid cavity,” *AIP Adv*, vol. 7, no. 1, 2017, doi: 10.1063/1.4974075.
- [28] F. Chen and D. Yao, “Realizing of plasmon Fano resonance with a metal nanowall moving along MIM waveguide,” *Opt Commun*, vol. 369, pp. 72–78, 2016, doi: 10.1016/j.optcom.2016.02.024.
- [29] M. Wang, M. Zhang, Y. Wang, R. Zhao, and S. Yan, “Fano resonance in an asymmetric MIM waveguide structure and its application in a refractive index nanosensor,” *Sensors (Switzerland)*, vol. 19, no. 4, 2019, doi: 10.3390/s19040791.
- [30] Z. Li *et al.*, “Control of Multiple Fano Resonances Based on a Subwavelength MIM Coupled Cavities System,” *IEEE Access*, vol. 7, pp. 59369–59375, 2019, doi: 10.1109/ACCESS.2019.2914466.
- [31] M. F. Hassan, M. M. Hasan, M. Radoan, and R. H. Sagor, “Design and Performance Analysis of an Ultra-compact Nano-plasmonic Refractive Index Sensor,” *2020 8th International Electrical Engineering Congress, iEECON 2020*, no. Mdm, 2020, doi: 10.1109/iEECON48109.2020.229582.
- [32] I. Tathfif, M. F. Hassan, K. S. Rashid, A. A. Yaseer, and R. H. Sagor, “A highly sensitive plasmonic refractive index sensor based on concentric triple ring resonator for cancer biomarker and chemical concentration detection,” *Opt Commun*, vol. 519, no. April, p. 128429, 2022, doi: 10.1016/j.optcom.2022.128429.
- [33] I. Tathfif, K. S. Rashid, A. A. Yaseer, and R. H. Sagor, “Alternative material titanium nitride based refractive index sensor embedded with defects: An emerging solution in sensing arena,” *Results Phys*, vol. 29, p. 104795, 2021, doi: 10.1016/j.rinp.2021.104795.

- [34] I. Munteanu and T. Weiland, “RF & Microwave Simulation with the Finite Integration Technique – From Component to System Design,” pp. 247–260, 2007, doi: 10.1007/978-3-540-71980-9_26.
- [35] T. Weiland, “Time domain electromagnetic field computation with finite difference methods,” *International Journal of Numerical Modelling: Electronic Networks, Devices and Fields*, vol. 9, no. 4, pp. 295–319, 1996, doi: 10.1002/(SICI)1099-1204(199607)9:4<295::AID-JNM240>3.0.CO;2-8.
- [36] Z. Rahimi, “The Finite Integration Technique (FIT) and the Application in Lithography Simulations,” p. 132, 2011, [Online]. Available: <https://opus4.kobv.de/opus4-fau/files/1788/PDFE.pdf>
- [37] J. B. S. L D Landau, J. S. Bell, M. J. Kearsley, L. P. Pitaevskii, E.M. Lifshitz, *Electrodynamics of Continuous Media*. 1984.
- [38] E. Palik, *Handbook of Optical Constants of Solids*. 1991.
- [39] W. Lai, K. Wen, J. Lin, Z. Guo, Q. Hu, and Y. Fang, “Plasmonic filter and sensor based on a subwavelength end-coupled hexagonal resonator,” *Appl Opt*, vol. 57, no. 22, p. 6369, Aug. 2018, doi: 10.1364/AO.57.006369.
- [40] S. Khani, M. Danaie, and P. Rezaei, “Tunable single-mode bandpass filter based on metal–insulator–metal plasmonic coupled U-shaped cavities,” *IET Optoelectronics*, vol. 13, no. 4, pp. 161–171, 2019, doi: 10.1049/iet-opt.2018.5098.
- [41] D. Barchiesi and T. Grosjes, “Fitting the optical constants of gold, silver, chromium, titanium, and aluminum in the visible bandwidth,” *J Nanophotonics*, vol. 8, no. 1, p. 083097, Jan. 2014, doi: 10.1117/1.JNP.8.083097.
- [42] H. Emami Nejad, A. Mir, and A. Farmani, “Supersensitive and Tunable Nano-Biosensor for Cancer Detection,” *IEEE Sens J*, vol. 19, no. 13, pp. 4874–4881, Jul. 2019, doi: 10.1109/JSEN.2019.2899886.
- [43] C.-B. Yu *et al.*, “Graphene oxide deposited microfiber knot resonator for gas sensing,” *Opt Mater Express*, vol. 6, no. 3, p. 727, Mar. 2016, doi: 10.1364/ome.6.000727.
- [44] M. A. Butt, S. N. Khonina, and N. L. Kazanskiy, “Metal-insulator-metal nano square ring resonator for gas sensing applications,” *Waves in Random and Complex Media*, vol. 31, no. 1. Taylor and Francis Ltd., pp. 146–156, 2021. doi: 10.1080/17455030.2019.1568609.
- [45] L. Ali, M. U. Mohammed, M. Khan, A. H. Bin Yousuf, and M. H. Chowdhury, “High-Quality Optical Ring Resonator-Based Biosensor for Cancer Detection,” *IEEE Sens J*, vol. 20, no. 4, pp. 1867–1875, Feb. 2020, doi: 10.1109/JSEN.2019.2950664.
- [46] D. Mohammad and K. Behnam, “Design of a label-free photonic crystal refractive index sensor for biomedical applications,” *Photonics Nanostruct*, vol. 31, pp. 89–98, Sep. 2018, doi: 10.1016/j.photonics.2018.06.004.

- [47] R. H. Sagor, M. F. Hassan, A. A. Yaseer, E. Surid, and M. I. Ahmed, “Highly sensitive refractive index sensor optimized for blood group sensing utilizing the Fano resonance,” *Applied Nanoscience (Switzerland)*, vol. 11, no. 2, pp. 521–534, 2021, doi: 10.1007/s13204-020-01622-5.
- [48] S. Chupradit *et al.*, “Ultra-sensitive biosensor with simultaneous detection (Of cancer and diabetes) and analysis of deformation effects on dielectric rods in optical microstructure,” *Coatings*, vol. 11, no. 12, 2021, doi: 10.3390/coatings11121564.
- [49] D. G. (Dominik G.) Rabus, *Integrated ring resonators : the compendium*. Springer, 2007.
- [50] X. P. Jin, X. G. Huang, J. Tao, X. S. Lin, and Q. Zhang, “A novel nanometric plasmonic refractive index sensor,” *IEEE Trans Nanotechnol*, vol. 9, no. 2, pp. 134–137, Mar. 2010, doi: 10.1109/TNANO.2009.2038909.
- [51] A. D. Rakic', R. Rakic', A. B. Djuriš, J. M. Elazar, and M. L. Majewski, “Optical properties of metallic films for vertical-cavity optoelectronic devices,” 1998.
- [52] T. Wu *et al.*, “A nanometric temperature sensor based on plasmonic waveguide with an ethanol-sealed rectangular cavity,” *Opt Commun*, vol. 339, pp. 1–6, Mar. 2015, doi: 10.1016/j.optcom.2014.11.064.
- [53] K. Niitsu, S. Ota, K. Gamo, H. Kondo, M. Hori, and K. Nakazato, “Development of Microelectrode Arrays Using Electroless Plating for CMOS-Based Direct Counting of Bacterial and HeLa Cells,” *IEEE Trans Biomed Circuits Syst*, vol. 9, no. 5, pp. 607–619, Oct. 2015, doi: 10.1109/TBCAS.2015.2479656.
- [54] X. Liang, Q. Zhang, and H. Jiang, “Quantitative reconstruction of refractive index distribution and imaging of glucose concentration using diffusing light,” *Optics InfoBase Conference Papers*, pp. 1–6, 2006, doi: 10.1364/bio.2006.sh38.
- [55] C. Y. Tan and Y. X. Huang, “Dependence of Refractive Index on Concentration and Temperature in Electrolyte Solution, Polar Solution, Nonpolar Solution, and Protein Solution,” *J Chem Eng Data*, vol. 60, no. 10, pp. 2827–2833, 2015, doi: 10.1021/acs.jced.5b00018.
- [56] C.-T. Chou Chao, Y.-F. Chou Chau, and H.-P. Chiang, “Biosensing on a Plasmonic Dual-Band Perfect Absorber Using Intersection Nanostructure,” *ACS Omega*, vol. 7, no. 1, pp. 1139–1149, Jan. 2022, doi: 10.1021/acsomega.1c05714.
- [57] X. J. Liang, A. Q. Liu, C. S. Lim, T. C. Ayi, and P. H. Yap, “Determining refractive index of single living cell using an integrated microchip,” *Sens Actuators A Phys*, vol. 133, no. 2, pp. 349–354, Feb. 2007, doi: 10.1016/j.sna.2006.06.045.
- [58] N. Ayyanar, G. Thavasi Raja, M. Sharma, and D. Sriram Kumar, “Photonic Crystal Fiber-Based Refractive Index Sensor for Early Detection of Cancer,” *IEEE Sens J*, vol. 18, no. 17, pp. 7093–7099, Sep. 2018, doi: 10.1109/JSEN.2018.2854375.